Stretch-Based Hyperelastic Material Formulations for Isogeometric Kirchhoff-Love Shells with Application to Wrinkling

Hugo M. Verhelst, Matthias M. Möller, Henk J den Besten, Angelos Mantzaflaris, Mirek L. Kaminski

Stretch-Based Hyperelastic Material Formulations for Isogeometric Kirchhoff-Love Shells with Application to Wrinkling

H.M. Verhelst[1,1], M. Möller[1], J.H. Den Besten[1], A. Mantzaflaris[1], M.L. Kaminski[1]

[a]*Delft University of Technology, Department of Maritime and Transport Technology, Mekelweg 2, Delft 2628 CD, The Netherlands*
[b]*Delft University of Technology, Department of Applied Mathematics, Van Mourik Broekmanweg 6, Delft 2628 XE, The Netherlands*
[c]*Inria Sophia Antipolis - Méditerranée, Université Côte d'Azur 2004 route des Lucioles - BP 93, 06902 Sophia Antipolis cedex, France*

Abstract

Modelling nonlinear phenomena in thin rubber shells calls for stretch-based material models, such as the Ogden model which conveniently utilizes eigenvalues of the deformation tensor. Derivation and implementation of such models have been already made in Finite Element Methods. This is, however, still lacking in shell formulations based on Isogeometric Analysis, where higher-order continuity of the spline basis is employed for improved accuracy. This paper fills this gap by presenting formulations of stretch-based material models for isogeometric Kirchhoff-Love shells. We derive general formulations based on explicit treatment in terms of derivatives of the strain energy density functions with respect to principal stretches for (in)compressible material models where determination of eigenvalues as well as the spectral basis transformations is required. Using several numerical benchmarks, we verify our formulations on invariant-based Neo-Hookean and Mooney-Rivlin models and with a stretch-based Ogden model. In addition, the model is applied to simulate collapsing behaviour of a truncated cone and it is used to simulate tension wrinkling of a thin sheet.

Keywords: isogeometric analysis, Kirchhoff-Love shell, stretch-based strain energy density, arc-length methods, wrinkling

1. Introduction

To model phenomena like wrinkling in membranes [1–5] or the deformation of biological tissues [6–8], thin shell formulations with non-linear hyperelastic material models are typically used. These material models are defined using a *strain energy (density) function*, which measures the strain energy stored in the material when deformed [9]. Material models with strain energy density functions based on the invariants (i.e. *invariant-based* models) of the deformation tensor, such as the Neo-Hookean or the Mooney-Rivlin formulations, have been widely used to study wrinkling or deformation of biological tissues. However, for rubber materials or living organs such as the liver, spine, skin, rectum, bladder or the aorta, material models defined by the eigenvalues and eigenvectors of the deformation tensor (i.e. *stretch-based* models) such as the Ogden, Sharriff or exponential and logarithmic models [10–12] provide better accuracy of material characteristics with respect to experimental tests [13–15].

To include hyperelastic material models into shell formulations, derivatives of the strain energy density function with respect to the components of the deformation tensor are required to define the stress and material tensors. For invariant-based models, this is generally a straight-forward exercise, since the invariants of the deformation tensor are defined in terms of the components of the deformation tensor. However, for stretch-based models, these derivatives result in stress and material tensors defined in the spectral basis (i.e. in terms of the eigenvectors), making incorporation of these models non-trivial. The first incorporation of stretch-based material models in the Finite Element Method (FEM) was obtained for axisymmetric problems [16, 17] and later the extension to generally shaped shells was made [8, 18, 19]. In these works, either closed-form expressions of the tangents of the principal stretches [17, 19] were obtained, or explicit computation of principal directions and values [16, 20, 21] was performed. In the former case, an unknown stretching parameter is used, which can be eliminated for incompressible models [22] and, in fact, imposes numerical difficulties when applied to compressible shells [22, 23]. In the latter case, principal directions and values need to be solved using an eigenvalue problem and a tensor transformation is required. However, for compressible materials no additional parameters are required.

With the advent of isogeometric analysis (IGA) [24], new spline-based shell formulations have been presented [25–27]. The advantage of these formulations is that the geometry is exactly preserved after discretization and that arbitrary continuity of the basis functions across element boundaries provides high convergence rates and allows for achieving necessary continuities in variational formulations, for instance leading to rotation-free Kirchhoff-Love shell formulations [25, 28]. These formulations have been used to advance the development of refinement splines [29] and to optimize shell structures [30], amongst other developments. A general hyperelastic isogeometric shell formulation has been developed for general compressible and incompressible material models [31] and specific formulations for biological membranes have been obtained [32]. Roohbakashan and Sauer [7] developed formulations to eliminate numerical through-thickness integration for hyperelastic Kirchhoff-Love shells. Isogeometric Kirchhoff-Love shell formulations are successfully used for biomedical applications to model aortic valve closure [33] and bioprosthetic heart valve dynamics [34, 35] as well as for industrial applications to perform buckling, vibration and nonlinear deformation analyses of composite wind turbine blades [36, 37]. However, all advances in [7, 31–34, 36] employ the derivatives of the strain energy density function with respect to the components of the deformation tensor, thus application of these works is possible for invariant-based models. On the other hand, stretch-based models such as the Ogden model require specific treatment of the spectral deformation tensor the existing generalized formulations. Contrary to the aforementioned developments in the FEM context, stretch-based material models have not yet been considered in isogeometric Kirchhoff-Love shell formulations.

In this paper we present mathematical formulations for the incorporation of stretch-based material models in the isogeometric Kirchhoff-Love shell model for (in)compressible material models. This enables the use of stretch-based material models such as the Ogden model together with the efficient Kirchhoff-Love shell formulation in isogeometric analysis, for application on wrinkling analysis or biomechanical simulations. The formulations

*Corresponding Author.
Email addresses: h.m.verhelst@tudelft.nl (H.M. Verhelst), m.moller@tudelft.nl (M. Möller), henk.denbesten@tudelft.nl (J.H. Den Besten), angelos.mantzaflaris@inria.fr (A. Mantzaflaris)

hold for material models defined for 3D continua which are integrated over the shell thickness. We employ explicit determination of the principal directions and values applicable to compressible and incompressible materials. The tensor transformation from the spectral to the curvilinear basis - which is needed for compatibility with existing codes - implies additional computational costs compared to a component-based formulation. These costs are minimised by using minor and major symmetry of the hyperelastic material tensor. Besides comparison with analytical solutions, the model is applied to simulate structural instabilities: the collapse of a truncated cone [19] and the wrinkling phenomenon in a stretched sheet. These instabilities are captured with (extended) arc-length methods [38, 39], combined with IGA [40]. The former simulation reveals the complex collapse behaviour of the truncated cone when using the arc-length method; something that was not reported in literature before. For the latter simulation, this paper reports the first IGA results for this case, compared to results from commercial FEM packages.

Following the introduction of notations, preliminary identities and the isogeometric Kirchhoff-Love shell formulation backgrounds (Section 2), we derive the stretch-based formulations including numerical procedures (Section 3) and discuss the isogeometric Kirchhoff-Love shell implementation aspects (Section 4). The model is benchmarked with analytical or reference solutions and it is applied to model the collapse behaviour of a truncated cone and the wrinkling formation in a stretched thin sheet in Section 5. Concluding remarks follow in Section 6.

2. The Kirchhoff-Love Shell Model

Using continuum mechanics and tensor calculus [41–43], the isogeometric Kirchhoff-Love formulations [7, 25, 31, 44] are briefly summarized. For more details and elaborate derivations reference is made to previous publications.

Firstly, Section 2.1 provides the notations that are used in this paper, as well as some preliminary tensor identities. Section 2.2 introduces the coordinate system and consequently the curvilinear basis that are used for the Kirchhoff-Love shell formulation. In Section 2.3 we provide the formulations of the shell kinematics, where the concepts of deformation and strain are defined. Lastly, Section 2.4 provides the variationel formulation of the Kirchhoff-Love shell, without specifying the constitutive relations, since those are covered in Section 3.

2.1. Notations and Preliminary Identities

For the ease of reference, the notations and preliminary identities are based on the ones used in [31]. Lower-case italic quantities (a) represent scalars, lower-case bold quantities ($\mathbf{a}$) denote vectors. Upper-case quantities denote two-dimensional quantities; italic and non-bold (A) for matrices, italic and bold for second-order tensors ($\boldsymbol{A}$). Third-order tensors are not used in the present work, and fourth-order tensors are represented by calligraphic capitals ($\mathbb{A}$). The following product operators are defined: inner product $\mathbf{a}\cdot\mathbf{b}$, cross-product $\mathbf{a}\times\mathbf{b}$ and tensor product $\mathbf{a}\otimes\mathbf{b}$. Furthermore, we represent covariant basis vectors with subscripts ($\mathbf{a}_i$) and contravariant vectors with superscript ($\mathbf{a}^j$). Latin indices take values $\{1,2,3\}$ whereas Greek ones take values $\{1,2\}$. By construction, $\mathbf{a}_i\cdot\mathbf{a}^j=\delta_i^j$, with δ_i^j the Kronecker delta. Second- and fourth-order tensors are denoted by $\boldsymbol{A}=A^{ij}\mathbf{a}_i\otimes\mathbf{a}_j=A_{ij}\mathbf{a}^i\otimes\mathbf{a}^j$ and $\mathbb{A}=\mathbb{A}^{ijkl}\mathbf{a}_i\otimes\mathbf{a}_j\otimes\mathbf{a}_k\otimes\mathbf{a}_l=\mathbb{A}_{ijkl}\mathbf{a}^i\otimes\mathbf{a}^j\otimes\mathbf{a}^k\otimes\mathbf{a}^l$, respectively, where A_{ij} and $\mathbb{A}_{ijkl}$ denote covariant components and A^{ij} and $\mathbb{A}^{ijkl}$ denote contravariant components.

The Einstein summation convention is adopted to represent tensor operations and when summations are unclear, it is explicitly mentioned. In this notation, the trace and determinant of a tensor are defined for tensor $\mathbf{A}=A_{ij}\,\mathbf{a}^i\otimes\mathbf{a}^j$ as in [31, 41, 42]

$$\operatorname{tr}\boldsymbol{A}=A_{ij}a^{ij}\quad\text{and}\quad\det\{\boldsymbol{A}\}=\left|A_{ij}\right|/\left|a_{ij}\right|,\tag{1}$$

where $\left|A_{ij}\right|$ denotes the determinant of the matrix A, $a^{ij}=\mathbf{a}^i\cdot\mathbf{a}^j$ and $a_{ij}=\mathbf{a}_i\cdot\mathbf{a}_j$. The inverse of a tensor $\boldsymbol{A}$ is denoted by $\boldsymbol{A}^{-1}$ or $\bar{\boldsymbol{A}}$. The derivative of the inverse and the determinant of a tensor, with respect to one of its components become:

$$\begin{aligned}&\frac{\partial\operatorname{tr}\boldsymbol{A}}{\partial A_{ij}}=a^{ij},\quad\frac{\partial\det\{\boldsymbol{A}\}}{\partial A_{ij}}=\det\{\boldsymbol{A}\}\bar{A}_{ij}\quad\text{and}\\&\frac{\partial\bar{\boldsymbol{A}}}{\partial A_{ij}}=-\frac{1}{2}\left\{A^{-1}_{ik}A^{-1}_{lj}+A^{-1}_{il}A^{-1}_{kj}\right\}.\end{aligned}\tag{2}$$

2.2. Shell Coordinate System

The Kirchhoff-Love shell element formulation is based on the Kirchhoff Hypothesis, that is, the cross-section does not shear and orthogonal vectors in the undeformed configuration remain orthogonal after deformation. As a consequence, any point in the shell can be represented by a point on the mid-surface and a contribution in normal direction:

$$\mathbf{x}=\mathbf{r}+\theta^3\mathbf{a}_3,\tag{3}$$

with the shell mid-surface $\mathbf{r}(\theta^1,\theta^2)$ and the unit normal direction $\mathbf{a}_3(\theta^3)$ for the deformed configuration $\mathbf{x}(\theta^1,\theta^2,\theta^3)$. For the undeformed configuration $\mathring{\mathbf{x}}$, the same relation holds with all quantities decorated with a $\mathring{\cdot}$. The parametrization utilizes surface coordinates θ^α and the through-thickness coordinate θ^3. Derivatives with respect to these coordinates are denoted by $(\cdot)_{,i}=\partial(\cdot)/\partial\theta^i$.

The covariant basis of the mid-surface is represented by $\mathbf{a}_i$

$$\mathbf{a}_\alpha=\frac{\partial\mathbf{r}}{\partial\theta^\alpha},\quad\mathbf{a}_3=\frac{\mathbf{a}_1\times\mathbf{a}_2}{|\mathbf{a}_1\times\mathbf{a}_2|},\tag{4}$$

and the first fundamental form is $a_{\alpha\beta}=\mathbf{a}_\alpha\cdot\mathbf{a}_\beta$. The curvature tensor $\mathbf{b}=b_{\alpha\beta}\,\mathbf{a}^\alpha\otimes\mathbf{a}^\beta$ is represented by the second fundamental form of surfaces, which can be obtained using the Hessian of the surface $\mathbf{a}_{\alpha,\beta}$ or the derivative of the normal vector $\mathbf{a}_{3,\alpha}$

$$b_{\alpha\beta}=\mathbf{a}_3\cdot\mathbf{a}_{\alpha,\beta}=-\mathbf{a}_{3,\beta}\cdot\mathbf{a}_\alpha.\tag{5}$$

The derivative of the normal vector is obtained by Weingarten's formula $\mathbf{a}_{3,\alpha}=-b^\beta_\alpha\mathbf{a}_\beta$ with $b^\beta_\alpha=a^{\alpha\gamma}b_{\gamma\beta}$ as the mixed curvature tensor [44]. Taking the derivative of Eq. (3), the covariant basis of the shell coordinate system $\mathbf{x}$ can be formulated as follows:

$$\mathbf{g}_\alpha=\mathbf{x}_{,\alpha}=\mathbf{a}_\alpha+\theta^3\mathbf{a}_{3,\alpha},\quad\mathbf{g}_3=\mathbf{x}_{,3}=\mathbf{a}_3.\tag{6}$$

The metric coefficients are constructed by taking the inner-product of these basis vectors, i.e.

$$g_{\alpha\beta}=\mathbf{g}_\alpha\cdot\mathbf{g}_\beta=a_{\alpha\beta}-2\theta^3b_{\alpha\beta}+\left(\theta^3\right)^2\mathbf{a}_{3,\alpha}\cdot\mathbf{a}_{3,\beta},\tag{7}$$

where in the second equality, Eq. (5) is used. Moreover, $g_{\alpha3}=0$ and $g_{33}=1$ [25]. Using the definition of the covariant metric g_{ij}, the contravariant metric g^{ij} and basis vectors $\mathbf{g}^i$ can be found:

$$g^{\alpha\beta}=[g_{\alpha\beta}]^{-1},\quad\mathbf{g}^\alpha=g^{\alpha\beta}\mathbf{g}_\beta.\tag{8}$$

The third contravariant basis vector $\mathbf{g}_3$ is again the normal vector $\mathbf{a}_3$ since it has unit-length by construction (see Eq. (4)).

Remark 1. *In the isogeometric Kirchhoff-Love shell formulations [25, 31], the last term in Eq. (7) is neglected because of the thin shell assumption, meaning $(\theta^3)^2$ takes small values. However, the co- and contravariant basis vectors ($\mathbf{g}_\alpha$ and $\mathbf{g}^\alpha$, respectively) are used in the mapping of the stretch-based material matrix onto the contravariant undeformed basis (Section 4.3). To enable an accurate comparison of the invariant-based and stretch-based formulation, we do not neglect the $O((\theta^3)^2)$ term, contrary to previous works [7, 31].*

2.3. Shell Kinematics

The deformed and undeformed configurations ($\mathbf{x}$ and $\mathring{\mathbf{x}}$, respectively) are related to each other by the mid-plane deformation vector $\mathbf{u}$ by $\mathbf{r} = \mathring{\mathbf{r}}+\mathbf{u}$ and $\mathbf{a}_3 = \mathbf{a}_3(\mathring{\mathbf{r}}+\mathbf{u})$. However, in both the invariant-based and stretch-based forms that are described in this paper, the deformations are defined using the undeformed and deformed geometries. In continuum mechanics, the deformation gradient $\mathbf{F}$ and the deformation tensor $\mathbf{C}$ are defined as [31, 43]:

$$\mathbf{F} = \frac{\mathrm{d}\mathbf{x}}{\mathrm{d}\mathring{\mathbf{x}}} = \mathbf{g}_i \otimes \mathring{\mathbf{g}}^i, \quad \mathbf{C} = \mathbf{F}^\top\mathbf{F} = \mathbf{g}_i \cdot \mathbf{g}_j\, \mathring{\mathbf{g}}^i \otimes \mathring{\mathbf{g}}^j = g_{ij}\, \mathring{\mathbf{g}}^i \otimes \mathring{\mathbf{g}}^j. \quad (9)$$

Note that the deformation tensor is defined in the contravariant undeformed basis $\mathring{\mathbf{g}}^i \otimes \mathring{\mathbf{g}}^j$. For Kirchhoff-Love shells, it is known that $g_{\alpha 3} = g_{3\alpha} = 0$, hence this implies $C_{\alpha 3} = C_{3\alpha} = 0$. Since $g_{33} = 1$, which implies C_{33} to be unity and meaning that the thickness remains constant under deformation. In hyperelastic Kirchhoff-Love shell formulations, the contribution of C_{33} is therefore incorporated by *static condensation*, where the correction of C_{33} is performed analytically for incompressible materials and iteratively for compressible materials. Therefore, we denote the deformation tensor $\mathbf{C}$ and its inverse $\bar{\mathbf{C}}$ as denoted as:

$$\mathbf{C} = g_{\alpha\beta}\, \mathring{\mathbf{g}}^\alpha \otimes \mathring{\mathbf{g}}^\beta + C_{33}\mathring{\mathbf{a}}_3 \otimes \mathring{\mathbf{a}}_3, \quad (10)$$

$$\bar{\mathbf{C}} = g^{\alpha\beta}\, \mathring{\mathbf{g}}_\alpha \otimes \mathring{\mathbf{g}}_\beta + \frac{1}{C_{33}}\mathring{\mathbf{a}}_3 \otimes \mathring{\mathbf{a}}_3. \quad (11)$$

From Eqs. (10) and (11), it can be observed that the thickness-contribution (index 3) is decoupled from the in-plane contributions (Greek indices α, β). This is a consequence of the Kirchhoff Hypothesis and therefore is only valid for Kirchhoff-Love shells. Consequently, using the definition $\tilde{\mathbf{C}} = g_{\alpha\beta}\, \mathring{\mathbf{g}}^\alpha \otimes \mathring{\mathbf{g}}^\beta$, the trace and determinant of $\mathbf{C}$ can be simplified accordingly [41, 42]:

$$\operatorname{tr}\mathbf{C} = \operatorname{tr}\tilde{\mathbf{C}} + C_{33} = g_{\alpha\beta}g^{\alpha\beta} + C_{33}, \quad (12)$$

$$\det\{\mathbf{C}\} = \det\{\mathbf{F}\}^2 = J^2 = \frac{\left|g_{\alpha\beta}\right|}{\left|\mathring{g}_{\alpha\beta}\right|}C_{33} = J_0^2 C_{33} = \lambda_1^2\lambda_2^2\lambda_3^2, \quad (13)$$

where J denotes the *Jacobian determinant* and J_0 is its in-plane counterpart. Furthermore, the tensor invariants of $\mathbf{C}$ simplify to:

$$I_1 := \operatorname{tr}\{\mathbf{C}\} = g_{\alpha\beta}\mathring{g}^{\alpha\beta} + C_{33} = \lambda_1^2 + \lambda_2^2 + \lambda_3^2, \quad (14)$$

$$I_2 := \frac{1}{2}\Big(\operatorname{tr}\{\mathbf{C}\}^2 - \operatorname{tr}\Big\{\mathbf{C}^2\Big\}\Big) = C_{33}g_{\alpha\beta}\mathring{g}^{\alpha\beta} + J_0^2$$
$$= \lambda_1^2\lambda_2^2 + \lambda_2^2\lambda_3^2 + \lambda_1^2\lambda_3^2, \quad (15)$$

$$I_3 := \det\{\mathbf{C}\} = \lambda_1^2\lambda_2^2\lambda_3^2, \quad (16)$$

where λ_i are the *principal stretches* of the shell and λ_i^2 are the eigenvalues of the deformation tensor $\mathbf{C}$. The squares of the eigenvalues are the roots of the characteristic polynomial:

$$(\lambda_i^2)^3 - I_1(\lambda_i^2)^2 + I_2\lambda_i^2 - I_3 = 0. \quad (17)$$

Corresponding eigenvectors are denoted by $\mathbf{v}_i$, which are normalized to have unit-length. The eigenvalue decomposition (or *spectral decomposition*) of the deformation tensor $\mathbf{C}$ can be written as [41, 42]:

$$\mathbf{C} = C_{ij}\mathring{\mathbf{g}}^i \otimes \mathring{\mathbf{g}}^j = \lambda_i^2 \mathbf{v}_i \otimes \mathbf{v}_i. \quad (18)$$

Where the Einstein summation convention is used. Since C_{33} is decoupled by construction, one can immediately see from Eqs. (10) and (18) that $\lambda_3 = \sqrt{C_{33}}$ and $\mathbf{v}_3 = \mathring{\mathbf{a}}_3$.

For the sake of completeness, we recall the definition of the Green-Lagrange strain tensor $\mathbf{E} = E_{\alpha\beta}\, \mathring{\mathbf{g}}^\alpha \otimes \mathring{\mathbf{g}}^\beta$ from [25, 31] and its decomposition to membrane and bending contributions (ε and κ, respectively):

$$E_{\alpha\beta} = \frac{1}{2}\Big(g_{\alpha\beta} - \mathring{g}_{\alpha\beta}\Big) = \frac{1}{2}\Big((a_{\alpha\beta} - \mathring{a}_{\alpha\beta}) - 2\theta^3\Big(b_{\alpha\beta} - \mathring{b}_{\alpha\beta}\Big)\Big) \quad (19)$$
$$= \varepsilon_{\alpha\beta} + \theta_3\kappa_{\alpha\beta}.$$

Remark 2. *Following up on Remark 1; the contribution of the $O((\theta^3)^2)$ term in Eq. (7) is neglected in the strain tensor and its derivatives. The $O((\theta^3)^2)$ term is only included in Eq. (7) to ensure equivalence in comparison of the stretch- and invariant-based formulations.*

2.4. Variational Formulation

The shell internal and external equilibrium equations in variational form are derived by the principle of virtual work [25, 31]. The variations of internal and external work are defined as:

$$\delta W(\mathbf{u}, \delta\mathbf{u}) = \delta W^{\mathrm{int}} - \delta W^{\mathrm{ext}}$$
$$= \int_\Omega \mathbf{n} : \delta\boldsymbol{\varepsilon} + \mathbf{m} : \delta\boldsymbol{\kappa}\, \mathrm{d}\Omega - \int_\Omega \mathbf{f} \cdot \delta\mathbf{u}\, \mathrm{d}\Omega\,, \quad (20)$$

with $\delta\mathbf{u}$ being the virtual displacement, $\delta\boldsymbol{\varepsilon}$ and $\delta\boldsymbol{\kappa}$ the virtual strain components, Ω the mid-surface and $\mathrm{d}\Omega = \sqrt{\left|\mathring{a}_{\alpha\beta}\right|}\mathrm{d}\theta^1\mathrm{d}\theta^2$ the differential area in the undeformed configuration, mapped to the integration domain $\Omega^* = [0,1]^2$ using the undeformed mid-plane measure. Furthermore, with slight abuse of notation, the tensors $\mathbf{n} = n^{\alpha\beta}\, \mathring{\mathbf{g}}_\alpha \otimes \mathring{\mathbf{g}}_\beta$ and $\mathbf{m} = m^{\alpha\beta}\, \mathring{\mathbf{g}}_\alpha \otimes \mathring{\mathbf{g}}_\beta$ denote the shell normal force and bending moment tensors, respectively, with

$$n^{\alpha\beta} = \int_{[-t/2,t/2]} S^{\alpha\beta}\, \mathrm{d}\theta^3\,, \quad m^{\alpha\beta} = \int_{[-t/2,t/2]} \theta^3 S^{\alpha\beta}\, \mathrm{d}\theta^3\,. \quad (21)$$

Here, $S^{\alpha\beta}$ denotes the coefficients of the stress tensor following from the constitutive relations that will be derived in Section 3 and t stands for the shell thickness. The total differentials of the stress resultants are:

$$\mathrm{d}n^{\alpha\beta} = \int_{[-t/2,t/2]} \mathbb{C}^{\alpha\beta\gamma\delta}\, \mathrm{d}\theta^3\, \mathrm{d}\varepsilon_{\gamma\delta} + \int_{[-t/2,t/2]} \mathbb{C}^{\alpha\beta\gamma\delta}\theta^3\, \mathrm{d}\theta^3\, \mathrm{d}\kappa_{\gamma\delta}\,,$$
$$\mathrm{d}m^{\alpha\beta} = \int_{[-t/2,t/2]} \mathbb{C}^{\alpha\beta\gamma\delta}\theta^3\, \mathrm{d}\theta^3\, \mathrm{d}\varepsilon_{\gamma\delta} + \int_{[-t/2,t/2]} \mathbb{C}^{\alpha\beta\gamma\delta}\Big(\theta^3\Big)^2\, \mathrm{d}\theta^3\, \mathrm{d}\kappa_{\gamma\delta}\,. \quad (22)$$

Discretizing the equations using known formulations from previous publications [25, 31, 44], the solution $\mathbf{u}$ is represented by a finite sum of weighted basis functions and the tensors $\mathbf{n}$, $\mathbf{m}$, $\boldsymbol{\varepsilon}$ and $\boldsymbol{\kappa}$ are linearized around the weights using Gateaux derivatives. The linearized tensors are denoted by $(\cdot)' = \frac{\partial(\cdot)}{\partial u_r}$ in the following, where u_r are individual weights of the solution vector. Note that $\mathbf{u}'$ denotes the basis functions [31]. Using the discretized system, the residual vector is defined by:

$$R_r = F_r^{\mathrm{int}} - F_r^{\mathrm{ext}} = \int_\Omega \mathbf{n} : \frac{\partial\boldsymbol{\varepsilon}}{\partial u_r} + \mathbf{m} : \frac{\partial\boldsymbol{\kappa}}{\partial u_r}\, \mathrm{d}\Omega - \int_\Omega \mathbf{f} \cdot \frac{\partial\mathbf{u}}{\partial u_r}\, \mathrm{d}\Omega\,, \quad (23)$$

and must be equal to the zero vector for the weights $\mathbf{u}$ corresponding to the exact solution. To solve the residual equation $\mathbf{R} = \mathbf{0}$, another linearization is performed, yielding the Jacobian matrix or *tangential stiffness matrix* K:

$$K_{rs} = K_{rs}^{\mathrm{int}} - K_{rs}^{\mathrm{ext}} \quad (24)$$
$$= \int_\Omega \frac{\partial\mathbf{n}}{\partial u_s} : \frac{\partial\boldsymbol{\varepsilon}}{\partial u_r} + \mathbf{n} : \frac{\partial^2\boldsymbol{\varepsilon}}{\partial u_r \partial u_s} + \frac{\partial\mathbf{m}}{\partial u_s} : \frac{\partial\boldsymbol{\kappa}}{\partial u_r} + \mathbf{m} : \frac{\partial^2\boldsymbol{\kappa}}{\partial u_r \partial u_s}\, \mathrm{d}\Omega$$
$$- \int_\Omega \frac{\partial\mathbf{f}}{\partial u_s} \cdot \frac{\partial\mathbf{u}}{\partial u_r}\, \mathrm{d}\Omega\,.$$

Note that the matrix contains a contribution for the external load depending on the solution vector ($\mathbf{f}(\mathbf{u})$). For instance, follower-pressures are defined by $\mathbf{f}(\mathbf{u}) = p\mathbf{n}(\mathbf{u})$, where $\mathbf{n}$ is the surface normal. In order to solve for nonlinear equation, Newton iterations are performed for solution $\mathbf{u}$ and increment $\Delta\mathbf{u}$ by solving

$$K\Delta\mathbf{u} = -\mathbf{R}. \tag{25}$$

3. Stretch-Based Constitutive Relations

Invariant-based (in)compressible material model formulations have been obtained for the strain energy density functions $\Psi(\mathbf{C})$ in component-form based on [31]. However, when experimental material data fitting is involved a formulation in terms of stretches (i.e. in terms of the eigenvalues of $\mathbf{C}$, $\Psi(\boldsymbol{\lambda})$ with $\boldsymbol{\lambda} = (\lambda_1, \lambda_2, \lambda_3)$ might be preferred, meaning that a transformation to spectral form is required. Therefore, this section provides the main contribution of this paper: the generalized formulations for the implementation of stretch-based material models in the isogeometric Kirchhoff-Love shell model. Throughout this section, reference is made to equations of [31] for comparison purposes.

The section is structured as follows: Section 3.1 provides the basics for the derivation of the stretch-based constitutive relations. Thereafter, Section 3.2 and Section 3.3 provide the derivations for incompressible and compressible material models, respectively, in the stretch-based formulations. These formulations are the novelty of the present paper.

3.1. General Relations

Assuming $\Psi(\boldsymbol{\lambda})$, we derive relations for the stress and material tensor in terms of the (normalized) eigenvector bases (Eq. (18)):

$$\mathbf{S} = \sum_{i,j=1}^{3} S^{ij}\, \mathbf{v}_i \otimes \mathbf{v}_j, \quad \mathbb{C} = \sum_{i,j,k,l=1}^{3} \mathbb{C}^{ijkl}\, \mathbf{v}_i \otimes \mathbf{v}_j \otimes \mathbf{v}_k \otimes \mathbf{v}_l. \tag{26}$$

These equations are valid for 3D continua and hence need to be modified to incorporate the through-thickness stress components. Reading Eq. (10), $C_{\alpha\beta} = g_{\alpha\beta}$ but $C_{33} \neq g_{33} = 1$ to avoid violation of the plane stress condition. To correctly incorporate the plane-stress condition ($S_{33} = 0$), the material tensor $\mathbb{C}$ is modified using static condensation, which implies that the material tensor $\hat{\mathbb{C}}$ corrected for plane-stress is defined by [31]:

$$\hat{\mathbb{C}}^{\alpha\beta\gamma\delta} = \mathbb{C}^{\alpha\beta\delta\gamma} - \frac{\mathbb{C}^{\alpha\beta 33}\mathbb{C}^{33\delta\gamma}}{\mathbb{C}^{3333}}. \tag{27}$$

For incompressible materials, this term is derived analytically using the incompressibility condition ($J = 1$) whereas for compressible materials, it is corrected iteratively.

When $\mathbf{S}$ and $\mathbb{C}$ are known, these tensors are transformed to the bases $\mathring{\mathbf{g}}_i \otimes \mathring{\mathbf{g}}_j$ and $\mathring{\mathbf{g}}_i \otimes \mathring{\mathbf{g}}_j \otimes \mathring{\mathbf{g}}_k \otimes \mathring{\mathbf{g}}_l$, respectively. This will be discussed in Section 4.3.

The derivative of any scalar function with respect to the deformation tensor $\mathbf{C}$ can be written as a derivative with respect to the stretch by applying the chain rule [41]:

$$\frac{\partial(\cdot)}{\partial\mathbf{C}} = \sum_{i=1}^{3} \frac{\partial(\cdot)}{\partial\lambda_i^2}\frac{\partial\lambda_i^2}{\partial\mathbf{C}} = \sum_{i=1}^{3} \frac{\partial(\cdot)}{\partial\lambda_i^2}\mathbf{v}_i \otimes \mathbf{v}_i = \sum_{i=1}^{3} \frac{1}{2\lambda_i}\frac{\partial(\cdot)}{\partial\lambda_i}\mathbf{v}_i \otimes \mathbf{v}_i. \tag{28}$$

From this, it follows that:

$$S^{ij} = \begin{cases} \dfrac{1}{\lambda_i}\dfrac{\partial\Psi}{\partial\lambda_i}, & i = j \\ 0, & i \neq j \end{cases} \tag{29}$$

which shows that the coefficients of the stress tensor are purely diagonal and we thus refer with S^{ii}, $i = 1, ..., 3$ to the non-zero components of $\mathbf{S}$.

Remark 3. *From Eq. (18) and Eq. (28), it follows that*

$$\frac{\partial\mathbf{C}}{\partial(\lambda_i^2)} = \mathbf{v}_i \otimes \mathbf{v}_i = \frac{\partial\lambda_i^2}{\partial\mathbf{C}}. \tag{30}$$

Due to the fact that the eigenvector basis with $\mathbf{v}_i$ is orthogonal and normalized (i.e. orthonormal), the product the basis vectors $\mathbf{v}_i$ span the identity tensor: $\mathbf{I} = \mathbf{v}_i \otimes \mathbf{v}_i$.

Furthermore, it can also be shown that for the material tensor, the following holds [17–19, 21, 41]:

$$\mathbb{C}^{ijkl} = \frac{1}{\lambda_k}\frac{\partial S^{ii}}{\partial\lambda_k}\delta_i^j\delta_k^l + \frac{S^{jj} - S^{ii}}{\lambda_j^2 - \lambda_i^2}(\delta_i^k\delta_j^l + \delta_i^l\delta_j^k)(1 - \delta_i^j). \tag{31}$$

where the indices (i, j, k, l) refer to specific components of the fourth-order material tensor, thus no summation over the indices is applied. The first part of $\mathbb{C}^{ijkl}$ represents the normal components (diagonal elements) and the second part denotes the shear components (off-diagonal elements). In the formulation of the component-based counterpart of this equation ([31, eq. 36]) these parts are not explicitly visible, since the spectral form by definition uses the principal directions of the deformation tensor, whereas shear and normal contributions are mixed in the curvilinear form of the material tensor. Note that for the second part of this equation, the case $\lambda_i = \lambda_j$ results in an undefined result. Hence, using L'Hopital's rule, this limit case can be identified:

$$\lim_{\lambda_j\to\lambda_i} \frac{S^{jj} - S^{ii}}{\lambda_j^2 - \lambda_i^2} = \lim_{\lambda_j\to\lambda_i} \frac{\frac{\partial S^{jj}}{\partial\lambda_j} - \frac{\partial S^{ii}}{\partial\lambda_j}}{2\lambda_j} = \frac{1}{2\lambda_i}\left(\frac{\partial S^{jj}}{\partial\lambda_j} - \frac{\partial S^{ii}}{\partial\lambda_j}\right). \tag{32}$$

Since $J = \lambda_1\lambda_2\lambda_3$, the derivatives of J are:

$$\frac{\partial J}{\partial\lambda_i} = \frac{J}{\lambda_i}, \quad \frac{\partial^2 J}{\partial\lambda_j\partial\lambda_j} = (1 - \delta_i^j)\frac{J}{\lambda_i\lambda_j}. \tag{33}$$

3.2. Incompressible Material Models

For incompressible materials, the incompressibility condition ($J = 1$) is enforced using a Lagrange multiplier p in the strain energy density function [31, 41]:

$$\Psi(\lambda_i) = \Psi_{el}(\lambda_i) - p(J - 1). \tag{34}$$

where Ψ_{el} is the original strain energy density function. Using Eq. (29), the stress tensor becomes:

$$S^{ii} = \frac{1}{\lambda_i}\left(\frac{\partial\Psi_{el}}{\partial\lambda_i} - \frac{\partial p}{\partial\lambda_i} - p\frac{\partial J}{\partial\lambda_i}\right). \tag{35}$$

Where again, we do not sum over repeated indices. Comparing S^{ii} with the component-based result in [31, eq. 41] shows that all components can easily be obtained using substitution in Eq. (28). To comply with the plane-stress condition ($S^{33} = 0$), the equation to be solved for the Langrange multiplier p using the incompressibility condition ($J = 1$) denotes:

$$\frac{1}{\lambda_3}\left(\frac{\partial\Psi_{el}}{\partial\lambda_3} - p\frac{\partial J}{\partial\lambda_3}\right) = 0, \tag{36}$$

which implies, using the derivative of J from Eq. (33):

$$p = \left(\frac{\partial J}{\partial\lambda_3}\right)^{-1}\frac{\partial\Psi_{el}}{\partial\lambda_3} = \lambda_3\frac{\partial\Psi_{el}}{\partial\lambda_3}. \tag{37}$$

It can easily be shown that Eq. (37) is similar to the expression of p in the component-based form [31, eq. 46] using $\lambda_3^2 = C_{33}$.

The derivative of the stress tensor with respect to the stretch is required to find the material tensor, as observed in Eq. (31). From Eq. (35) it follows that:

$$\begin{aligned}\frac{\partial S^{ii}}{\partial \lambda_j} &= \frac{\partial}{\partial \lambda_j}\left(\frac{1}{\lambda_i}\frac{\partial \Psi}{\partial \lambda_i}\right) = \frac{1}{\lambda_i}\frac{\partial^2 \Psi}{\partial \lambda_i \partial \lambda_j} - \delta_i^j \frac{1}{\lambda_i^2}\frac{\partial \Psi}{\partial \lambda_i} \\ &= \frac{1}{\lambda_i}\Bigg(\frac{\partial^2 \Psi_{el}}{\partial \lambda_i \partial \lambda_j} - \frac{\partial p}{\partial \lambda_i}\frac{\partial J}{\partial \lambda_j} - \frac{\partial p}{\partial \lambda_j}\frac{\partial J}{\partial \lambda_i} \\ &\quad - p\frac{\partial^2 J}{\partial \lambda_i \partial \lambda_j} - \delta_i^j \frac{1}{\lambda_i}\left(\frac{\partial \Psi_{el}}{\partial \lambda_i} - p\frac{\partial J}{\partial \lambda_i}\right)\Bigg),\end{aligned} \tag{38}$$

where the incompressibility condition ($J = 1$) is used again and where no summation over repeated indices is applied. Note that the Kronecker delta δ_i^j covers the case when $i = j$. The derivative of p follows from Eq. (37) and reads:

$$\frac{\partial p}{\partial \lambda_i} = \lambda_3 \frac{\partial^2 \Psi_{el}}{\partial \lambda_3 \partial \lambda_i} + \delta_i^3 \frac{\partial \Psi_{el}}{\partial \lambda_3}. \tag{39}$$

Again, this result can be compared to its component-based counterpart in [31, eq. 47] and using Eq. (28) it can be observed that these equations are similar. Substituting Eqs. (33), (37) and (39) and $J = 1$ into Eqs. (35) and (38) then yields:

$$S^{\alpha\alpha} = \frac{1}{\lambda_\alpha}\left(\frac{\partial \Psi_{el}}{\partial \lambda_\alpha} - \frac{\lambda_3}{\lambda_\alpha}\frac{\partial \Psi_{el}}{\partial \lambda_3}\right), \tag{40}$$

$$\begin{aligned}\frac{\partial S^{\alpha\alpha}}{\partial \lambda_\beta} &= \frac{1}{\lambda_\alpha}\Bigg[\frac{\partial^2 \Psi_{el}}{\partial \lambda_\alpha \partial \lambda_\beta} - \frac{1}{\lambda_\beta}\left(\lambda_3 \frac{\partial^2 \Psi_{el}}{\partial \lambda_3 \partial \lambda_\alpha} + \delta_\alpha^3 \frac{\partial \Psi_{el}}{\partial \lambda_3}\right) \\ &\quad - \frac{1}{\lambda_\alpha}\left(\lambda_3 \frac{\partial^2 \Psi_{el}}{\partial \lambda_3 \partial \lambda_\beta} + \delta_\beta^3 \frac{\partial \Psi_{el}}{\partial \lambda_3}\right) - \lambda_3 \frac{\partial \Psi_{el}}{\partial \lambda_3}\frac{(1-\delta_\alpha^\beta)}{\lambda_\alpha \lambda_\beta} \\ &\quad - \delta_\alpha^\beta \frac{1}{\lambda_\alpha}\left(\frac{\partial \Psi_{el}}{\partial \lambda_\alpha} - \frac{1}{\lambda_\alpha}\lambda_3 \frac{\partial \Psi_{el}}{\partial \lambda_3}\right)\Bigg].\end{aligned} \tag{41}$$

Here, we do not apply summation over repeated indices. Comparison with the invariant-based formulation shows that λ_i^{-1} in front of the second term in Eq. (40) translates to $\bar{C}^{ij}$ in [31, eq. 49]. Using these identities, the material tensor can be derived from Eq. (31). For the static condensation term, reference is made to Eq. (27), hence the components $\mathbb{C}^{\alpha\beta 33}$, $\mathbb{C}^{33\alpha\beta}$ and $\mathbb{C}^{3333}$ need to be evaluated. From Eq. (31) it follows that:

$$\mathbb{C}^{\alpha\beta 33} = \frac{1}{\lambda_3}\frac{\partial S^{\alpha\alpha}}{\partial \lambda_3}\delta_\alpha^\beta = -\frac{1}{\lambda_3 \lambda_\alpha^2}\left[\lambda_3 \frac{\partial^2 \Psi_{el}}{\partial \lambda_3^2} + 2\frac{\partial \Psi_{el}}{\partial \lambda_3}\right]\delta_\alpha^\beta, \tag{42}$$

$$\mathbb{C}^{33\gamma\delta} = \frac{1}{\lambda_\gamma}\frac{\partial S^{3}}{\partial \lambda_\gamma}\delta_\gamma^\delta = -\frac{1}{\lambda_3 \lambda_\gamma^2}\left[\lambda_3 \frac{\partial^2 \Psi_{el}}{\partial \lambda_3^2} + 2\frac{\partial \Psi_{el}}{\partial \lambda_3}\right]\delta_\gamma^\delta, \tag{43}$$

$$\mathbb{C}^{3333} = \frac{1}{\lambda_3}\frac{\partial S^{3}}{\partial \lambda_3} = -\frac{1}{\lambda_3^3}\left[\lambda_3 \frac{\partial^2 \Psi_{el}}{\partial \lambda_3^2} + 2\frac{\partial \Psi_{el}}{\partial \lambda_3}\right], \tag{44}$$

such that the static condensation term becomes:

$$\frac{\mathbb{C}^{\alpha\beta 33}\mathbb{C}^{33\gamma\delta}}{\mathbb{C}^{3333}} = -\frac{\frac{1}{\lambda_3^2 \lambda_\alpha^2 \lambda_\gamma^2}\left[\lambda_3 \frac{\partial^2 \Psi_{el}}{\partial \lambda_3^2} + 2\frac{\partial \Psi_{el}}{\partial \lambda_3}\right]^2}{\frac{1}{\lambda_3^3}\left[\lambda_3 \frac{\partial^2 \Psi_{el}}{\partial \lambda_3^2} + 2\frac{\partial \Psi_{el}}{\partial \lambda_3}\right]}\delta_\alpha^\beta \delta_\gamma^\delta \tag{45}$$

$$= -\frac{1}{\lambda_\alpha^2 \lambda_\gamma^2}\left[\lambda_3 \frac{\partial^2 \Psi_{el}}{\partial \lambda_3^2} + 2\frac{\partial \Psi_{el}}{\partial \lambda_3}\right]\delta_\alpha^\beta \delta_\gamma^\delta. \tag{46}$$

Using this result, the in-plane incompressible material tensor can be evaluated as:

$$\begin{aligned}\mathbb{C}^{\alpha\beta\gamma\delta} &= \frac{1}{\lambda_\gamma}\frac{\partial S^{\alpha\alpha}}{\partial \lambda_\gamma}\delta_\alpha^\beta \delta_\gamma^\delta + \frac{S^{\beta\beta} - S^{\alpha\alpha}}{\lambda_\beta^2 - \lambda_\alpha^2}(\delta_\alpha^\gamma \delta_\beta^\delta + \delta_\alpha^\delta \delta_\beta^\gamma)(1 - \delta_\alpha^\beta) \\ &\quad - \frac{1}{\lambda_\alpha^2 \lambda_\gamma^2}\left[\lambda_3 \frac{\partial^2 \Psi_{el}}{\partial \lambda_3^2} + 2\frac{\partial \Psi_{el}}{\partial \lambda_3}\right]\delta_\alpha^\beta \delta_\gamma^\delta,\end{aligned} \tag{47}$$

where the second term should be replaced by Eq. (32) if $\lambda_\alpha = \lambda_\beta$.

3.3. Compressible Material Models

For compressible models, the Jacobian determinant J is not necessarily equal to 1. As a consequence, the deformation gradient $\mathbf{F}$ and deformation tensor $\mathbf{C}$ are modified such that $\mathbf{F}$ and $\mathbf{C}$ are a multiplicative decomposition of a volume-changing (*dilational*) part depending on J and a volume preserving (*distortional*) part depending on the modified deformation gradient and deformation tensors, $\dot{\mathbf{C}}$ and $\dot{\mathbf{F}}$, respectively [45]:

$$\dot{\mathbf{F}} = J^{-\frac{1}{3}}\mathbf{F}, \quad \dot{\mathbf{C}} = J^{-\frac{2}{3}}\mathbf{C}. \tag{48}$$

The modified deformation gradient and deformation tensor have determinants which are equal to 1 (corresponding to volume preservation), meaning:

$$\det\left\{\dot{\mathbf{F}}\right\} = \dot{\lambda}_1 \dot{\lambda}_2 \dot{\lambda}_3 = 1, \quad \det\left\{\dot{\mathbf{C}}\right\} = 1, \tag{49}$$

where the modified principal stretches $\dot{\lambda}_i$ are defined as:

$$\dot{\lambda}_i = J^{-\frac{1}{3}}\lambda_i. \tag{50}$$

Consequently, the invariants of the modified deformation tensor $\dot{\mathbf{C}}$ become:

$$\dot{I}_1 = J^{-2/3} I_1, \quad \dot{I}_2 = J^{-4/3} I_2, \quad \dot{I}_3 = 1, \tag{51}$$

with I_i the invariants of the deformation tensor $\mathbf{C}$. With $\dot{\mathbf{F}}, \dot{\mathbf{C}}$ and $\dot{I}_k$ as defined above, the strain energy density function $\Psi(\mathbf{C})$ for a compressible material can be described in a decoupled form, separating the response in a isochoric (or distortional) elastic part $\Psi_{\text{iso}}(\dot{\boldsymbol{\lambda}})$ and an volumetric (or dilational) elastic part $\Psi_{\text{vol}}(J)$ [41, 42, 45]:

$$\Psi(\boldsymbol{\lambda}) = \Psi_{\text{iso}}(\dot{\boldsymbol{\lambda}}) + \Psi_{\text{vol}}(J). \tag{52}$$

The volumetric elastic part Ψ_{vol} is required to be strictly convex and equal to zero if and only if $J = 1$ and $\dot{\mathbf{C}} = \mathbf{I}$ [41].

For compressible materials, the plane stress condition is incorporated by solving $S_{33} = 0$ for C_{33} using Newton linearizations [31, 46]:

$$S^{33} + \frac{1}{2}\mathbb{C}^{3333}\Delta C_{33} = 0, \tag{53}$$

where C_{33} is incrementally updated by $C_{33}^{(n+1)} = C_{33}^{(n)} + \Delta C_{33}^{(n)}$ with the increment on iteration n:

$$\Delta C_{33}^{(n)} = -2\frac{S_{(n)}^{33}}{\mathbb{C}_{(n)}^{3333}}. \tag{54}$$

In each iteration, the updated stress tensor $\mathbf{S}$ and material tensor $\mathbb{C}$ can be computed and iterations are continued until the plane stress condition is satisfied within a certain tolerance, i.e. $\left|S^{33}\right| <$ tol. When converged, static condensation can be performed for the material tensor using Eq. (27). Rather than using $C_{33}^{(0)} = 1$ [31], $C_{33}^{(0)} = J_0^{-2}$ is used for incompressible materials, although the difference for the two approaches is negligible.

Using Eq. (50), any volumetric strain energy density function for incompressible materials can be transformed to its compressible material equivalent by substituting Eq. (50) into Eq. (52) and by selecting a volumetric component Ψ_{vol}. Static condensation (Eq. (27)) is performed before transforming the material tensor.

4. Implementation Aspects

In this section, we recall the assembly of the nonlinear system for isogeometric Kirchhoff-Love shells (Section 4.1) as well as the computation of the eigenvalues and eigenvectors of the deformation tensor $\mathbf{C}$ (Section 4.2). Then we provide details about the transformation of the stress and material tensors $\mathbf{S}$ and $\mathbb{C}$ from spectral to curvilinear bases (Section 4.3).

4.1. System Assembly

For the implementation of Kirchhoff-Love shells recall that the vector of internal forces and the tangential stiffness matrix read [25, 31]:

$$F_r^{\text{int}} = \int_\Omega \left(\bar{\mathbf{n}}^\top \frac{\partial \bar{\varepsilon}}{\partial u_r} + \bar{\mathbf{m}}^\top \frac{\partial \bar{\kappa}}{\partial u_r} \right) \mathrm{d}\Omega \,, \tag{55}$$

$$K_{rs} = \int_\Omega \left(\left(\bar{\mathbf{D}}^0 \frac{\partial \bar{\varepsilon}}{\partial u_s} + \bar{\mathbf{D}}^1 \frac{\partial \bar{\kappa}}{\partial u_s} \right) \frac{\partial \bar{\varepsilon}}{\partial u_r} + \bar{\mathbf{n}}^\top \frac{\partial^2 \bar{\varepsilon}}{\partial u_r \partial u_s} \right. \tag{56}$$

$$\left. + \left(\bar{\mathbf{D}}^1 \frac{\partial \bar{\varepsilon}}{\partial u_s} + \bar{\mathbf{D}}^2 \frac{\partial \bar{\kappa}}{\partial u_s} \right) \frac{\partial \bar{\varepsilon}}{\partial u_r} + \bar{\mathbf{m}}^\top \frac{\partial^2 \bar{\kappa}}{\partial u_r \partial u_s} \right) \mathrm{d}\Omega \,. \tag{57}$$

Here, we note that the matrices $\bar{\mathbf{D}}^k$, $k = 0, 1, 2$, are k^{th} thickness moments of the material tensor represented as a 3×3 matrix and $\bar{\mathbf{n}}$ and $\bar{\mathbf{m}}$ are the zero-th and first thickness moments of the stress tensor, see [31]. The thickness integrals are, in the present paper and in [31], computed using numerical through-thickness integration with four Gaussian points. As discussed in [7], the matrices $\bar{\mathbf{D}}^1$ can differ in the variations of the normal force tensor $\bar{\mathbf{n}}$ and the moment tensor $\bar{\mathbf{m}}$ depending the analytic projected or directly decoupled alternatives for thickness integration.

4.2. Eigenvalue Computation

The eigenvalues of tensor quantity can be computed by solving Eq. (17) or, alternatively, by computing the eigenvalues of the matrix that results from computation of $\mathbf{C} = C_{ij}\, \mathring{\mathbf{g}}^i \otimes \mathring{\mathbf{g}}^j$ including the outer product. Since $\lambda_3^2 = \sqrt{C_{33}}$ is decoupled by construction, it suffices to compute λ_1^2 and λ_2^2 by computing the eigenvectors and eigenvalues of the 3×3 matrix following from computation of $\mathbf{C} = C_{\alpha\beta} \mathring{\mathbf{g}}_\alpha \otimes \mathring{\mathbf{g}}_\beta$. This computation results in three eigenpairs (eigenvalues and eigenvector) of which one eigenpair contains the zero-vector due to the decoupled construction. The other two eigenpairs ($\lambda_\alpha \in \mathbb{R}, \mathbf{v}_\alpha \in \mathbb{R}^3$) are the in-plane principle stretches and their directions.

4.3. Tensor Transformation

Since the stretch-based stress and material tensor are derived in spectral form (i.e. in the eigenvector space) a transformation towards the curvilinear basis needs required in order to use these entities in further computations. Recall that the spectral forms of $\mathbf{S}$ and $\mathbb{C}$ are:

$$\mathbf{S} = \sum_{i=1}^{3} S^{ii}\, \mathbf{v}_i \otimes \mathbf{v}_i, \quad \mathbb{C} = \sum_{i,j,k,l=1}^{3} \mathbb{C}^{ijkl}\, \mathbf{v}_i \otimes \mathbf{v}_j \otimes \mathbf{v}_k \otimes \mathbf{v}_l. \tag{58}$$

The invariant-based stress and material tensors are defined in the curvilinear basis, as follows:

$$\mathbf{S} = \sum_{i,j=1}^{3} S^{ij}\, \mathring{\mathbf{g}}_i \otimes \mathring{\mathbf{g}}_j \quad \mathbb{C} = \sum_{i,j,k,l=1}^{3} \mathbb{C}^{ijkl}\, \mathring{\mathbf{g}}_i \otimes \mathring{\mathbf{g}}_j \otimes \mathring{\mathbf{g}}_k \otimes \mathring{\mathbf{g}}_l. \tag{59}$$

Since the strain tensors (c.f. Eq. (19)) are defined in the curvilinear basis, it is convenient to define the quantities in the variational form (c.f. Eq. (20)) defined in the curvilinear basis. Hence, the stretch-based stress and material tensors are transformed to the undeformed covariant curvilinear basis by:

$$\begin{aligned} \tilde{S}^{ij} &= \sum_{p,q=1}^{3} S^{pq} (\mathbf{v}_p \cdot \mathring{\mathbf{g}}^i)(\mathbf{v}_q \cdot \mathring{\mathbf{g}}^j), \\ \tilde{\mathbb{C}}^{ijkl} &= \sum_{p,q,r,s=1}^{3} \mathbb{C}^{pqrs} (\mathbf{v}_p \cdot \mathring{\mathbf{g}}^i)(\mathbf{v}_q \cdot \mathring{\mathbf{g}}^j)(\mathbf{v}_r \cdot \mathring{\mathbf{g}}^k)(\mathbf{v}_s \cdot \mathring{\mathbf{g}}^l), \end{aligned} \tag{60}$$

where $\tilde{S}^{ij}$ and $\tilde{\mathbb{C}}^{ijkl}$ are the coefficients of the stress and material tensors in the curvilinear basis.

Obviously, the tensor transformation only needs to be computed for non-zero components of $\mathbb{C}^{pqrs}$. For incompressible material models, the plane-stress correction for C_{33} is applied analytically, which implies that the transformations only need to be applied for indices ranging from $\alpha, \beta, \gamma, \delta = 1, 2$, thus the transformation consists of mapping $2^4 = 16$ entries. However, it is known that for hyperelastic materials the contravariant components of the material tensor, $\mathbb{C}^{ijkl}$, posses minor and major symmetry [41, 42], i.e.

$$\mathbb{C}^{abcd} = \mathbb{C}^{bacd} = \mathbb{C}^{abdc} \qquad \text{minor symmetry}, \tag{61}$$

$$= \mathbb{C}^{cdab} \qquad \text{major symmetry}, \tag{62}$$

so that only six unique components exists for the $2 \times 2 \times 2 \times 2$ tensor. Furthermore, Eq. (31) implies that the non-zero components of $\mathbb{C}^{ijkl}$ are of the form $\mathbb{C}^{iiii}$, $\mathbb{C}^{iijj}$, $\mathbb{C}^{ijij}$ and $\mathbb{C}^{ijji}$ of which the last two are equal by virtue of the minor symmetry property. This implies that the $2 \times 2 \times 2 \times 2$ tensor has only four uniquely defined components, namely $\mathbb{C}^{1111}$, $\mathbb{C}^{1122}$, $\mathbb{C}^{2222}$ and $\mathbb{C}^{1212}$.

For compressible material models, the static condensation term is computed in the spectral basis, i.e. on the tensor $\mathbb{C}$ before it is transformed to the covariant undeformed tensor basis. From Eq. (54) we see that the iterative procedure to find C_{33} requires the computation of $\mathbb{C}^{3333}$, $\mathbb{C}^{\alpha\beta 33}$ and $\mathbb{C}^{33\alpha\beta}$, where the last two are equal by virtue of the major symmetry property. Reusing the minor and major symmetries, the computation is reduced to four distinct components, namely $\mathbb{C}^{1133}$, $\mathbb{C}^{2233}$, $\mathbb{C}^{1233}$ and $\mathbb{C}^{3333}$.

Accordingly, it can be concluded that for incompressible materials four and for compressible materials eight unique components of the spectral material tensor need to be computed, when exploiting minor and major symmetry, as well as the nature of Eq. (31). In summary, the transformations give rise to certain additional costs, which can be limited, however, by exploiting symmetry properties efficiently.

5. Numerical experiments

For benchmarking purposes, the results of four numerical experiments have been used for verification and validation of the presented formulations for incompressible and compressible material models. For the uniaxial tension and pressurized balloon benchmarks (Sections 5.1 and 5.2, respectively), analytical solutions are available, therefore they will serve as verification of the stretch-based material model formulations. Combining the present method with (extended) arc-length methods, we investigate the collapsing behaviour of a truncated conical shell [19] (Section 5.3) and we simulate wrinkling of a stretched thin sheet (Section 5.4).

In order to verify the presented isogeometric Kirchhoff-Love formulation for a stretch-based Ogden material with its FEM couterpart, the conical shell collapse (Section 5.3) is incorporated. Finally, we will apply our approach to model wrinkling of a thin sheet subject to tension. Our models have been implemented in the open-source library G+Smo (Geometry + Simulation Modules) [47, 48] and download and installation instructions to reproduce the data presented in the following are provided in the Supplementary Material.

In the numerical experiments, compressible and incompressible formulations of the Neo-Hookean (NH), Mooney-Rivlin (MR) and Ogden (OG) material models have been used. The

Neo-Hookean models are given by (compressible and incompressible, respectively):

$$\Psi(\mathbf{C}) = \frac{\mu}{2}\Big(J^{-\frac{2}{3}} I_1 - 3\Big) + \Psi_{\text{vol}}(J), \tag{63}$$

$$\Psi(\mathbf{C}) = \frac{\mu}{2}(I_1 - 3). \tag{64}$$

The Mooney-Rivlin models are given by [49, 50] (compressible and incompressible, respectively):

$$\Psi(\mathbf{C}) = \frac{c_1}{2}\Big(J^{-\frac{2}{3}} I_1 - 3\Big) + \frac{c_2}{2}\Big(J^{-\frac{4}{3}} I_2 - 3\Big) + \Psi_{\text{vol}}(J), \tag{65}$$

$$\Psi(\mathbf{C}) = \frac{c_1}{2}(I_1 - 3) + \frac{c_2}{2}(I_2 - 3). \tag{66}$$

For Ogden models, the following formulations are used (compressible and incompressible, respectively):

$$\Psi(\boldsymbol{\lambda}) = \sum_{p=1}^{N} \frac{\mu_p}{\alpha_p} J^{-\frac{1}{3}}\Big(\lambda_1^{\alpha_p} + \lambda_2^{\alpha_p} + \lambda_3^{\alpha_p} - 3\Big) + \Psi_{\text{vol}}(J), \tag{67}$$

$$\Psi(\boldsymbol{\lambda}) = \sum_{q=1}^{3}\left(\sum_{p=1}^{N} \frac{\mu_p}{\alpha_p}(\lambda_q^{\alpha_p} - 1)\right). \tag{68}$$

For all models, the following volumetric part of the strain energy density function is adopted:

$$\Psi_{\text{vol}} = K\mathcal{G}(J) = K\beta^{-2}\Big(\beta \log(J) + J^{-\beta} - 1\Big). \tag{69}$$

To check consistency of invariant based models (i.e. the NH and MR models), the invariants can be replaced by Eqs. (14) to (16) to obtain stretch-based forms, which is thus equivalent to the component-based form from [31]. Unless stated otherwise, for the compressible models $\beta = -2$, and for the Mooney-Rivlin model $c_1/c_2 = 7$ [50] is used. For the Ogden model the coefficients from [51] are re-scaled to the value of μ:

$$\begin{aligned} \mu_1 &= \frac{6.300}{\mu_0}\mu, \quad & \alpha_1 &= 1.3, \\ \mu_2 &= \frac{0.012}{\mu_0}\mu, \quad & \alpha_2 &= 5.0, \\ \mu_3 &= -\frac{0.100}{\mu_0}\mu, \quad & \alpha_3 &= -2.0, \end{aligned} \tag{70}$$

where $\mu_0 = 4.225$.

5.1. Uniaxial Tension

The first benchmark case is uniaxial tension of a material block. A block with dimensions $L \times W \times t = 1 \times 1 \times 0.001$ [m^3] is considered. The shear modulus is $\mu = E/(2(1+\nu))$ where E and ν are the Young's modulus and Poisson ratio, respectively, such that $\mu = 1.5 \cdot 10^6$[N/m^2]. The block is modeled by shell elements, i.e. the $L \times W$ plane is considered and all edges are restrained in vertical direction ($z = 0$). The left edge ($x = 0$) is restrained in x direction and on the right edge ($x = L$) a distributed load σt is applied. The bottom edge ($y = 0$) is restrained in y direction and the top edge ($y = B$) is free to move (see Fig. 1).

In Fig. 2 the results for uniaxial tension are depicted. For both compressible and incompressible materials, the analytical solution for the Cauchy stress are obtained from [41, ex. 1]. The numerical and analytical solutions for incompressible and compressible materials show a perfect match for all quantities studied (thickness decrease λ_3, axial Cauchy stress σ and Jacobian determinant J). Note that the Jacobian determinant for incompressible materials is equal to 1 and hence not shown. The residual norms of the non-linear iteration convergence for the invariant-based and stretch-based Neo-Hookean and Mooney-Rivlin models as well as the stretch-based Ogden model are equal in all iterations (see Table 1), showing that the present formulation provides exactly the same rates of convergence as the invariant-based method. Last but not least, Newton iterations converge with optimal speed (second-order convergence rate).

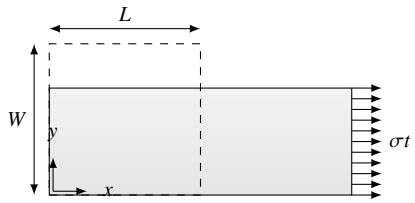

Figure 1: Geometry for the uniaxial tension case. The filled geometry represents the undeformed configuration and the dashed line indicates the undeformed geometry. The bottom side of the undeformed sheet is fixed in y-direction and the left side of the sheet is fixed in x-direction. The applied load is σt where σ is the actual Cauchy stress and t is the thickness of the sheet.

Table 1: Residual norms per iteration for the 10$^{\text{th}}$ load-step for uniaxial tension for all material models in compressible and incompressible forms. For the Neo-Hookean and Mooney-Rivlin models, the iteration residuals are provided for the stretch-based and invariant-based approaches. For the Ogden model, only the results for the stretch-based formulations are given, since no invariant-based formulation exists. For the Neo-Hookean and Mooney-Rivlin models, results are only observed in the last iteration, due to machine precision of the arithmetic. The Supplementary Material provides instructions to reproduce this table.

It.	Neo-Hookean		Mooney-Rivlin		Ogden
	Stretch	Invariant	Stretch	Invariant	Stretch
	Incompressible				
1	$2.033 \cdot 10^{-4}$	$2.033 \cdot 10^{-4}$	$4.021 \cdot 10^{-3}$	$3.999 \cdot 10^{-3}$	$4.442 \cdot 10^{-2}$
2	$1.129 \cdot 10^{-6}$	$1.129 \cdot 10^{-6}$	$2.248 \cdot 10^{-5}$	$2.253 \cdot 10^{-5}$	$1.313 \cdot 10^{-6}$
3	$3.575 \cdot 10^{-11}$	$3.575 \cdot 10^{-11}$	$7.106 \cdot 10^{-10}$	$7.229 \cdot 10^{-10}$	$4.149 \cdot 10^{-11}$
4	$2.554 \cdot 10^{-16}$	$6.929 \cdot 10^{-16}$	$5.088 \cdot 10^{-16}$	$1.776 \cdot 10^{-15}$	$1.602 \cdot 10^{-16}$
	Compressible				
1	$1.617 \cdot 10^{-3}$	$1.617 \cdot 10^{-3}$	$2.100 \cdot 10^{-3}$	$2.100 \cdot 10^{-3}$	$5.215 \cdot 10^{-3}$
2	$2.296 \cdot 10^{-7}$	$2.296 \cdot 10^{-7}$	$2.890 \cdot 10^{-6}$	$2.890 \cdot 10^{-6}$	$1.759 \cdot 10^{-7}$
3	$9.443 \cdot 10^{-13}$	$9.440 \cdot 10^{-13}$	$1.344 \cdot 10^{-11}$	$1.344 \cdot 10^{-11}$	$2.584 \cdot 10^{-13}$
4	$1.153 \cdot 10^{-15}$	$1.252 \cdot 10^{-16}$	$1.115 \cdot 10^{-15}$	$1.988 \cdot 10^{-16}$	$1.625 \cdot 10^{-15}$

5.2. Pressurized Balloon

The response affected pressure of a spherical balloon is used for benchmarking purposes as well. The analytical pressure formulation is obtained from [41, eq. 6.132]. The numerical model results are based on follower pressures, i.e. $\mathbf{f} = p_0 \mathbf{a}_3$ where $\mathbf{a}_3$ is the unit normal in the current configuration. The balloon is modeled as a quarter of a hemi-sphere, of which the bottom point is fixed in all directions, and on the sides a symmetry condition is applied by clamping the sides in normal direction and restriction deflections orthogonal to the symmetry boundary (see Fig. 3). The geometry is modelled by 2 elements over the height and 2 elements over the quarter-circumference, both of quadratic order.

For $R = 10$ [m], $t = 0.1$ [m] and $\mu = 4.2255 \cdot 10^5$ [N/m^2], a perfect agreement is obtained for all presented material models in comparison to the analytical solutions Fig. 4.

In Table 2 we represent the total CPU times related to system assembly for different material models for different mesh refinement levels and quadratic order for $p_0 = 10^4$. The assembly times for both the invariant-based formulations and for the stretch-based formulations are given for the Neo-Hookean and Mooney-Rivlin material models, whereas the stretch-based formulation is only available for the Ogden model. The total number of nonlinear iterations is the same in all cases, and so is the number of assembly operations. The table shows that the stretch-based formulations are slower than the invariant-based formulations, which is expected by the requirement for the transformation of the basis of the deformation tensor. It can also be seen that the Ogden model requires significantly more CPU time than the other models, which is due to the large number of terms in the strain energy density function.

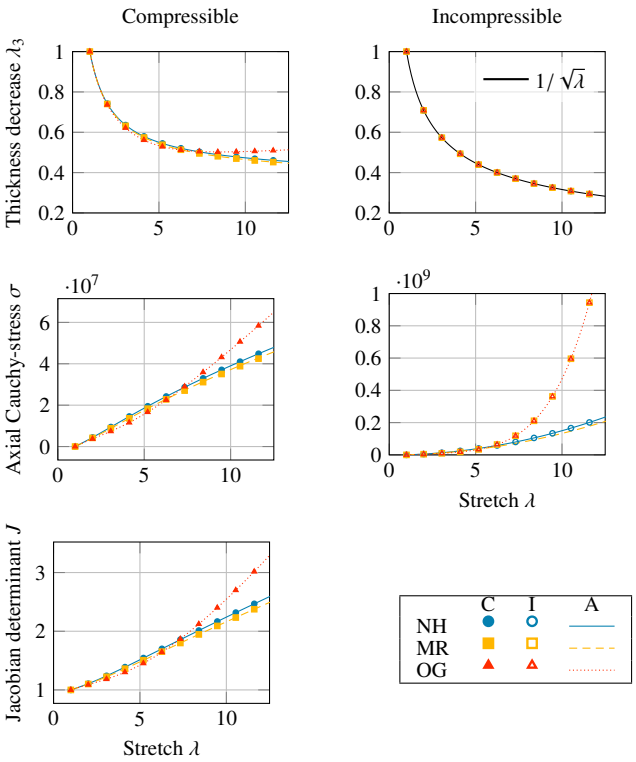

Figure 2: Results for uniaxial tension for compressible (C, left column) and incompressible materials (I, right column); where the first row presents the thickness decrease λ_3, the second row the axial Cauchy stress or true axial stress σ and the last row the Jacobian determinant J for compressible materials; all against the stretch λ. The material models that are used are the Neo-Hookean (NH) the Mooney-Rivlin (MR) and the Ogden (OG) material models and comparison is made to analytical (A) solutions from [41, ex. 1]. The Supplementary Material provides instructions to reproduce these figures.

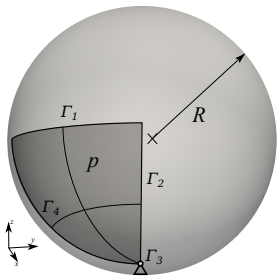

Figure 3: Geometry of the inflated balloon with 4 quadratic elements. Symmetry conditions are applied on the boundaries Γ_1, Γ_2 and Γ_4, which means that rotations around these boundaries and displacements in-plane normal to the boundaries are fixed. The bottom of the balloon (Γ_3) is an edge with a radius of 0.01 and is fixed in all directions.

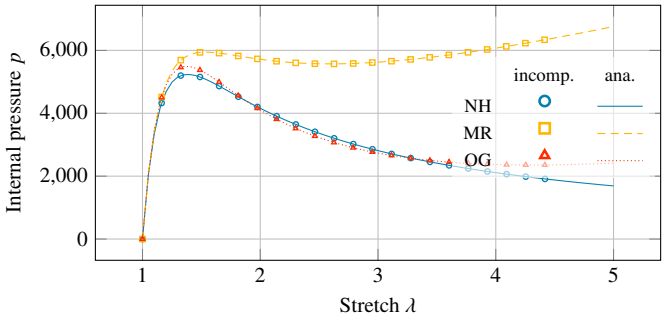

Figure 4: Inflation of a balloon. The vertical axis depicts the internally applied pressure and the horizontal axis depicts the stretch $\lambda_1 = \lambda_2 = \lambda$. The different lines and markers represent different material models, including Neo-Hookean (NH), Mooney-Rivlin (MR) and Ogden (OG). The radius of the sphere is $R = 10$ [m] and the thickness of the sphere $t = 0.1$ [m]. The Supplementary Material provides instructions to reproduce this figure.

Table 2: Total CPU assembly times (seconds) for the different material models (invariant-based where applicable) for different mesh sizes (#El.) for the inflated balloon benchmark. All results are obtained for the incompressible material models.

#El.	Neo-Hookean		Mooney-Rivlin		Ogden
	Invariant	Stretch	Invariant	Stretch	
1	0.18	0.13	0.18	0.13	0.41
4	0.42	0.28	0.43	0.29	1.07
16	1.42	0.93	1.45	0.94	3.95
64	6.19	4.55	6.69	4.35	18.49
256	40.67	26.77	44.10	28.60	119.65

5.3. *Conical Shell Collapse*

A collapsing conical shell (or *frustrum*) is presented as a benchmark for modelling of strong non-linearities [19]. A conical shell with height $H = 1$ [m], top radius $r = 1$ [m], bottom radius $R = 2$ [m] and thickness $t = 0.1$ [m] as depicted in Fig. 5 is considered. Since the reference solution models the frustrum axisymmetrically, a quarter of the geometry is modelled with 32 quadratic elements over the height and one quadratic element over the quarter-circumference to represent axial symmetry. The corresponding material model is of the Ogden type and has the following parameters:

$$\mu_1 = 6.300\ [\mathrm{N/m^2}], \qquad \alpha_1 = 1.3,$$
$$\mu_2 = 0.012\ [\mathrm{N/m^2}], \qquad \alpha_2 = 5.0,$$
$$\mu_3 = -0.100\ [\mathrm{N/m^2}], \qquad \alpha_3 = -2.0,$$

implying that $\mu = 4.225$ [N/m^2]. Two sets of boundary conditions are considered for this geometry. In both sets the bottom of the shell (Γ_2) is hinged, hence the displacements are restricted in all directions. The top shell edge (Γ_1) is either kept rigid (no x and y displacements) or free, referred to as *constant* or *variable* radius, respectively [19]. On the top edge, a uniform load p is applied, providing a uniform displacement Δ. Due to symmetry, only one quarter of the geometry is modelled, which means that symmetry boundary conditions are applied on the $x = 0$ and $y = 0$ planes (Γ_3, Γ_4, see Fig. 5); restricting in-plane deformations normal to the boundaries and restricting rotations on the boundary by applying clamped boundary conditions as described in [25]. The quarter-conical shell is modelled with 32 quartic shell elements over the width.

Loads are applied using displacement-control (DC) or arc-length control. In the former case, displacements are applied on the top-side of the cone and the deformation of the cone as well as the corresponding load on the top-boundary are computed. In the latter case, Crisfield's spherical arc-length procedure [38] is used with extensions for resolving complex roots [52, 53]. If this method does not converge to an equilibrium point, the step size is bisected until a converged step is found. After this step, the step size is reset to its original value [40].

Figs. 6 and 7 present the result of the collapsing conical shell (constant and variable radius, respectively) of the present study and the reference results from [19]. The results for the displacement-controlled (DC) solution procedure shows that the difference between the used material models are negligible, since the actual strains are relatively small. The results also agree with the displacement-controlled reference results of [19], and minor differences between the results might be a result of FE shear locking as involved for the reference results. Since more steps have been used for the displacement-controlled calculations, sharp corners in the curve can be observed for $\Delta \sim 1.9$ for constant radius and $\Delta \sim 1.8$ for variable radius.

An arc-length based calculation was used as well. From the results, one can observe revelation of the collapsing mechanism of the conical shell. For both cases (constant and variable radius) an almost anti-symmetric pattern in the load-deflection space can be observed, which initiates and finishes at the kinks in the curve that was found with the displacement-control procedure. For the

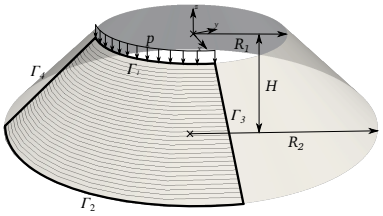

Figure 5: Geometry of the collapsing conical shell with 32 quadratic elements over the height.

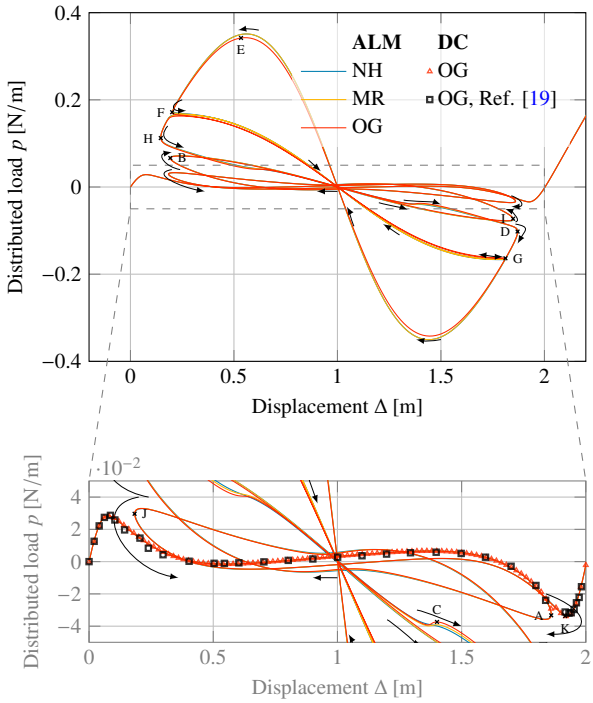

(a) Load-displacement diagram.

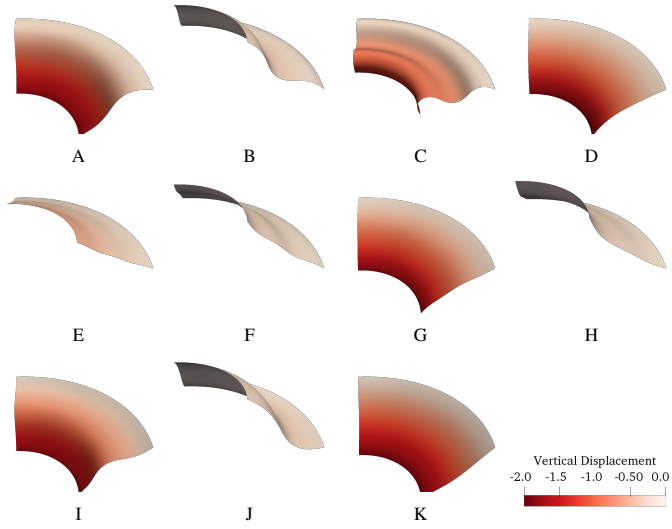

(b) Intermediate states of the frustrum

Figure 6: Result of the collapsing conical shell with *constant* radius;(a) load-displacement diagram,(b) undeformed geometries matching with the points indicated with capital letters in the diagram. The lines represent solutions obtained using the Arc-Length Method (ALM) and the markers represent solutions obtained by Displacement Control (DC). Note that the solution for the NH and MR models are overlapping on most parts of the path. The material models are Neo-Hookean (NH), Mooney-Rivlin (MR) and Ogden (OG). Since variation between the material models is rather small for the DC solutions, only the results for the OG material model are given. The reference results are obtained from [19]. A movie of the collapse (video 1) and instructions to reproduce the data are given as Supplementary Material.

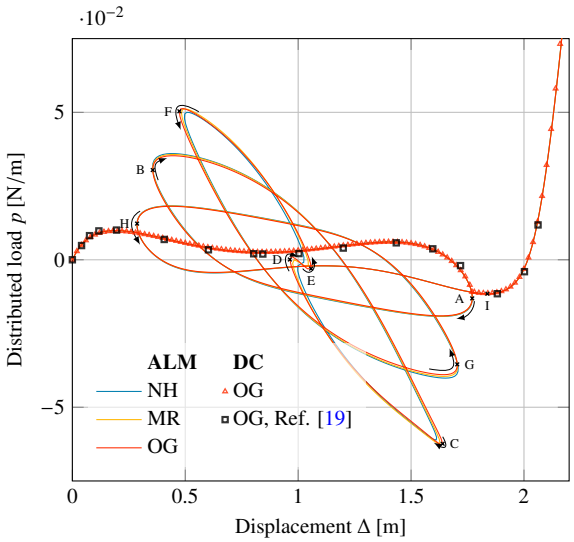

(a) Load-displacement diagram

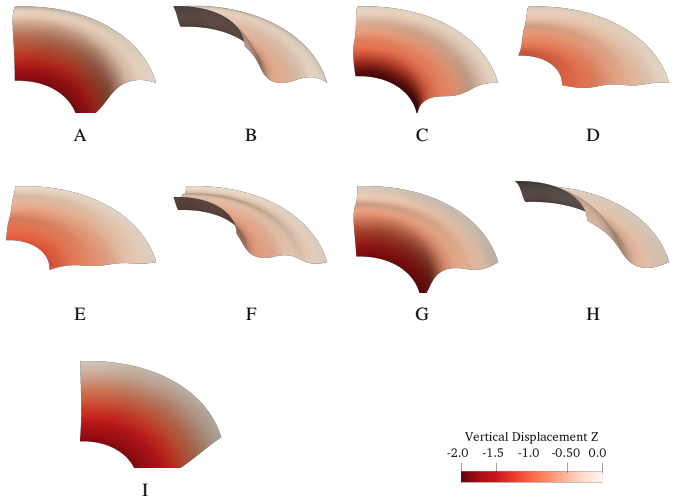

(b) Intermediate states of the frustrum

Figure 7: Result of the collapsing conical shell with *variable* radius; (a) load-displacement diagram, (b) undeformed geometries matching with the points indicated with capital letters in the diagram. The lines represent solutions obtained using the Arc-Length Method (ALM) and the markers represent solutions obtained by Displacement Control (DC). The material models are Neo-Hookean (NH), Mooney-Rivlin (MR) and Ogden (OG). Since variation between the material models is rather small for the DC solutions, only the results for the OG material model are given. The reference results are obtained from [19]. A movie of the collapse (video 2) and instructions to reproduce the data are given as Supplementary Material.

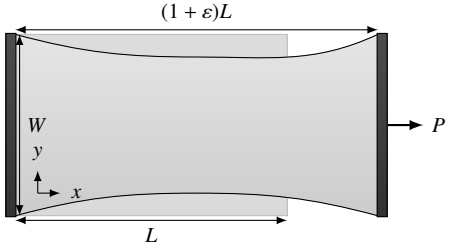

Figure 8: Modeling geometry for the uniaxially loaded restrained sheet.

constant-radius shell, Fig. 6a shows two loops of large magnitude. In Figs. 6b and 7b it can be seen that collapsing behaviour of the conical shell consists of states in which multiple *waves* in radial direction occur. For both cases, it can be seen that after the loops with the highest force-amplitude, the shell and its collapse-path invert and continue on the path that can be obtained with displacement-control.

To the best of the authors' knowledge, the collapsing of a conical shell was not investigated before. Complex load-displacement paths from Figs. 6a and 7a show that displacement-controlled simulations in this case ignore the collapsing behaviour of the shell with multiple limit points. The authors highly encourage further investigations on this benchmark for verification and validation.

5.4. Wrinkling of a stretched sheet

As an application of the model, we consider the wrinkling phenomenon of a stretched, thin membrane (see Fig. 11). Scaling laws based on experiments were first published in [1, 2] and analytical formulations related to this problem were established in [54]. Numerical results to this problem have been established for sheets with different aspect ratios β and different dimensionless thickness α [3–5, 55–59]. In most numerical studies, Neo-Hookean or Mooney-Rivlin models were used to model the wrinkling phenomenon, since strains usually reach high values (typically $\varepsilon \sim 10 - 50\%$). In this paper, we model tension wrinkling for the sake of benchmarking using incompressible Neo-Hookean, Mooney-Rivlin and Ogden models and Isogeometric Kirchhoff-Love shells, which is a novelty to the best of the authors' knowledge. In the first part of this section, the model is benchmarked on a restrained sheet without wrinkling formation and material parameter determination is performed. Thereafter, the results of wrinkling simulations are presented.

Material test

Related to the first benchmark in the work of [7] and on the experiments of [3], a tensile load is applied on a strip of which the short edges are fixed and the long edges are free (see Fig. 8). Focus is on the non-domensional load versus end-point displacement in longitudinal (load and displacement) direction.

Firstly, for the geometric parameters, $L = 9$[mm], $W = 3$[mm] and $t = 0.3$ [mm] are used, leading to $L/W = 3$ and $t/W = 0.1$. The material has Poisson's ratio $\nu = 0.5$ and for the NH material model a Young's modulus of $E = 30$ [kPa] is involved and for the MR material model one of $E = 90$ [kPa] leading to, $\mu = 10$ [kPa] and $\mu = 30$ [kPa], respectively. For the MR model, $c_1/c_2 = 1/2$ such that $c_1 = 1/9$ and $c_2 = 2/9$. Scaling according to Eq. (70) is applied for the Ogden material model and 8×8 quadratic elements are used. A good match with the results of the directly decoupled method of [7] for the incompressible Neo-Hookean and Mooney-Rivlin models can be observed in Fig. 9a. Note that the forces in the reference paper are normalized by $E = 3c_1$ for both the Neo-Hookean and Mooney-Rivlin models, whereas in the present simulations, the forces are normalized by $E = 3\mu$ (since $\nu = 0.5$ in the comparison with [7]).

In Fig. 10, we provide convergence plots of the present model (NH and OG stretch-based models) with respect to the relative error in the strains given a nondimensional load of $P/EA = 0.5$. The errors are plotted with respect to the Richardson extrapolation from the three finest meshes, since analytical solutions to the problem are not available. The results obtained for the NH model obtained from the invariant-based form are exactly the same and hence not provided here. The figures show that the convergence of the method is around second-order, independent of the order of the spline basis. Reference papers [7, 31] do not provide estimates of the order of convergence for the invariant-based material models or convergence plots for similar simulations. Hence, further comparison and investigations on the order of convergence for such membrane-dominated responses for shells with nonlinear material models are recommended.

Secondly, we compare our numerical model to the experimental results from a similar setup as depicted in Fig. 8 [3]. The corresponding geometric parameters are $L = 280$ [mm],

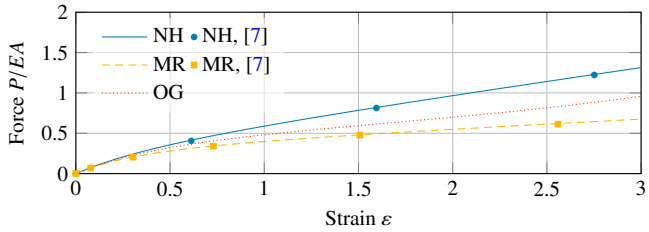

(a) Benchmarking results comparing to [7]. The reference results are obtained numerically.

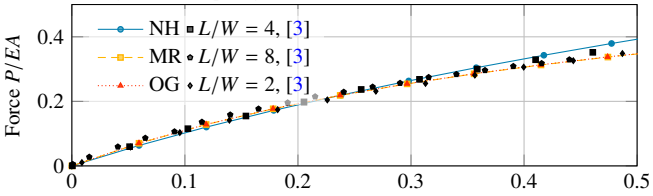

(b) Benchmarking results for comparison with [3]. Experimental results are depicted by markers for different aspect ratios L/W of the sheet. Numerical results from [3] are not included since they are indistinquishable from the present MR results.

Figure 9: Uniaxial tension of a restrained sheet using incompressible material models. The dimensionless force is obtained by normalization of the applied force P by the Young's modulus E and the cross sectional area A. The Supplementary Material provides instructions to reproduce these figures.

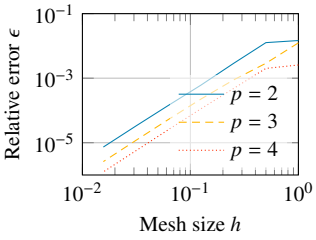

(a) Neo-Hookean (NH): the orders of convergence following from Richardson extrapolation are 2.11 ($p = 2$), 2.15 ($p = 3$) and 2.17 ($p = 4$).

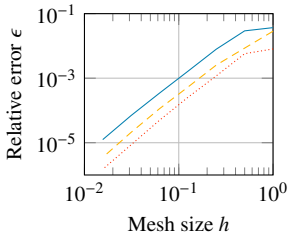

(b) Ogden (OG): the orders of convergence following from Richardson extrapolation are 2.27 ($p = 2$), 2.40 ($p = 3$) and 2.52 ($p = 4$).

Figure 10: Convergence rate of the restrained sheet under uniaxial tension with values from [7] for different material models (a-b). The error is relative error $\epsilon = |\varepsilon_{\text{num}} - \varepsilon_R|/\varepsilon_R$ where ε_{num} is the numerical value of the strain and ε_R is the Richardson-extrapolated value of the strain related to the last three meshes, all for a dimensionless force $P/EA = 0.5$. The orders of convergence following from the Richardson extrapolation are provided in the captions below the subfigures. The Supplementary Material provides instructions to reproduce the strain data.

$W = 140$ [mm] and $t = 0.14$ [mm], leading to $L/W = 2$ and $t/W = 10^3$. The material models are incompressible and for the NH material model, a parameter $\mu = 1.91 \cdot 10^5$ [Pa] is used, while for the MR model the parameters $c_1 = 3.16 \cdot 10^5$ [Pa] and $c_2 = 1.24 \cdot 10^5$ [Pa] are used. The results are depicted in Fig. 9b, from which it can be seen that there is an excellent agreement between the numerical results from [3] (obtained using the ABAQUS S4R element) and with the experimental results. In addition, the depicted fit for the Ogden material model was found, using parameters $\alpha_1 = 1.1$ [-], $\mu_1 = 1.0\mu_0$ [Pa], $\alpha_2 = -7$ [-], $\mu_2 = -0.003\mu_0$ [Pa], $\alpha_3 = -3$ [-] and $\mu_3 = -0.4\mu_0$ [Pa] with $\mu_0 = 1.91 \cdot 10^5$ Pa.

Wrinkling simulations

For the wrinkling simulations, we follow the work of [3] with the same parameters for the Mooney-Rivlin and Ogden models as in Fig. 9b. The model setup for the wrinkling simulations is depicted in Fig. 11. The modeling domain is depicted in the shaded area and surrounded by boundaries Γ_k, $k = 1, .., 4$. Firstly, the boundary Γ_1 is free, meaning that no displacement constraints are involved. Furthermore, the boundary at Γ_2 is clamped (matching the adjacent control points parallel to the symmetry axes) and displacements in y-direction and out-of-plane displacements are restricted. The displacements in x-direction are all equal over Γ_2.

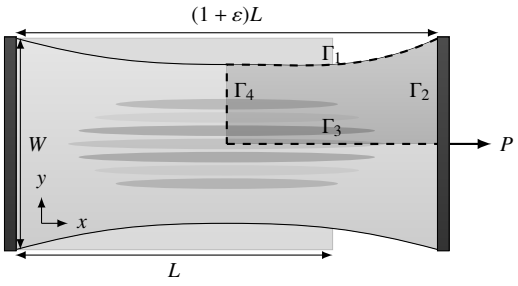

Figure 11: Modeling geometry for the wrinkled sheet.

Symmetry is imposed over Γ_4 by *clamping* the edges and by restricting deformations orthogonal to the axes ($u_x = 0$). Lastly, anti-symmetry is imposed over Γ_3 by restricting displacements in vertical direction and orthogonal to the boundary ($u_y = 0$). Similar to [3], we apply a anti-symmetry condition over Γ_3 since the symmetric and anti-symmetric wrinkling patterns can appear at the same critical load [5, 57]. For continuation, Crisfield's spherical arc-length method [38] is used with an extension for approaching bifurcation points [39], branch switching [60] and complex-root resolving [52, 53], all summarised and applied to IGA in [40].

Furthermore, for comparison, results from LS-DYNA (R11.0) and ANSYS (R19.1) simulations are presented for the same geometry and a Mooney-Rivlin model with the same parameters, however $\nu = 0.499$ in the LS-DYNA simulations since incompressible materials ($\nu = 0.5$) are not implemented. A displacement control approach is employed with an initial perturbation based on the first buckling mode corresponding to a tension load situation, perturbed with a factor of 10^{-4}. In LS-DYNA, the Hughes-Liu, the Hughes-Liu selective/reduced and the fully integrated shell elements are used, all with 4 quadrature points through-thickness and a shear correction factor equal to zero [61]. The results for the ANSYS SHELL181 element [62] are obtained using default options, which includes reduced integration and hour-glassing control. For both the LS-DYNA and ANSYS simulations, mesh refinements were applied until convergence.

From Fig. 12a large difference between the different solvers and between the material models can be observed. Firstly, it can be concluded that the MR results from the Isogeometric Kirchhoff-Love shell correspond most with the results obtained with LS-DYNA. Additionally, these results show good correspondence with the experimental results both in the low strain regime (until $\varepsilon \sim 0.08$) as well as towards restabilization of the wrinkles (between $\varepsilon \sim 0.2$ and $\varepsilon \sim 0.3$), only the maximum amplitude is slightly underestimated and the restabilization point (i.e. the point where the wrinkles vanish again) is predicted too early. Secondly, it can be observed that there is a large difference between the results from IGA or LS-DYNA and from ANSYS. Although different shell options in the FEA libraries have been varied (e.g. reduced/full integration, shear correction factors), the origin of these differences is yet unknown to the authors and requires further investigations. Lastly, significant differences between the Ogden and Mooney-Rivlin results can be observed, although the similarities in the material behaviour in Fig. 9b. From this it can be concluded that material fitting possibly needs to be done using experimental tests of different loading configurations, e.g. testing the bending response of the material.

6. Conclusions and recommendations

This paper provides mathematical formulations to accurately and efficiently model thin rubbers and several biological tissues by combining stretch-based material formulations such as the Ogden material model and smooth spline formulations of the Isogeometric Kirchhoff-Love shell. The formulations apply to compressible and incompressible material models and are based on an eigenvalue computation to obtain the principal stretches and their direction (i.e. the spectral basis). The spectral stress and material tensors are transformed to the curvilinear basis accordingly with limited computational costs due to tensor symmetries.

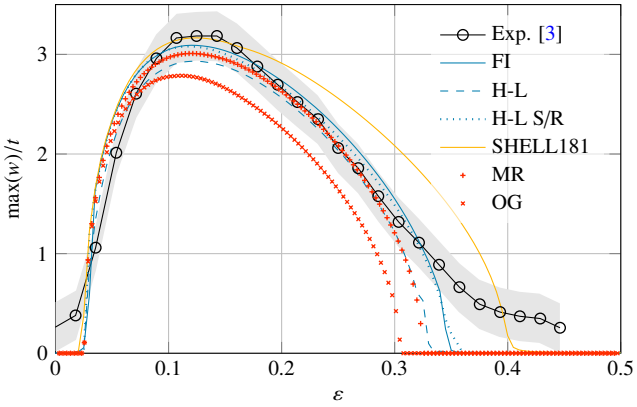

(a) Strain-amplitude diagram of the tension wrinkling of a thin sheet. The vertical axis represents the maximum amplitude normalized by the shell thickness t and the horizontal axis represents the strain ε of the sheet. The present model is used to obtain the Mooney-Rivlin (MR) and Ogden (OG) results. The fully integrated (FI), Hughes-Liu (H-L) and Hughes-Liu Selective/Reduced (H-L S/R) results are obtained using LS-DYNA and the SHELL181 results are obtained using ANSYS.

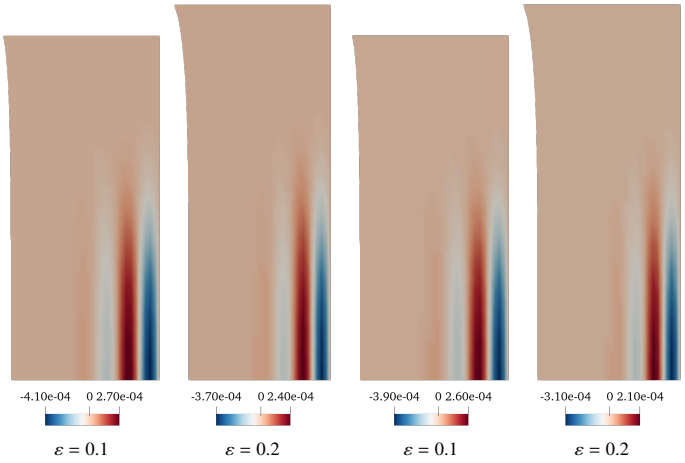

(b) Contour plot of out-of-plane displacements w for different strains ε for the MR model.

(c) Contour plot of out-of-plane displacements w for different strains ε for the OG model.

Figure 12: Wrinkling formation in a thin sheet subject to tension. The Supplementary Material provides instructions to reproduce these figures.

The results from numerical experiments with Neo-Hookean and Mooney-Rivlin material models, which can be represented in terms of invariants as well as in terms of stretches, shows that identical iteration residuals and correct Newton-convergence rates have been obtained. This confirms that the stretch-based and invariant-based shell formulations are equivalent. For these models it is also shown that the present formulation leads to higher CPU times due to the projection of the stress and material tensor; therefore, the advantage of the present formulation is mainly related to stretch-based material models (e.g. the Ogden model) and not to models that can be expressed explicitly in terms of the curvilinear tensor components of the deformation tensor (e.g. the invariant-based Neo-Hookean and Mooney Rivlin models). The analytical benchmarks have shown very good agreements confirming that the formulations and implementation are correct.

Employing (extended) arc-length methods in combination with the present model, we investigated the collapsing behaviour of a truncated conical shell and the wrinkling behaviour of a stretched thin sheet. In case of the collapsing truncated conical shell, the Ogden model was used in combination with either displacement controlled or arc-length controlled loads on the top boundary. The displacement controlled results show good agree-

ment with reference results from literature. Using the arc-length method, the previously unnoticed response of the cone during collapse was obtained, while overlapping with the displacement controlled results on the stable part of the equilibrium path.

We also used the present formulations to model the phenomenon of wrinkling of a stretched thin sheet. To the best of the authors' knowledge, such simulations have only been published for finite element methods and not with Ogden material models. Hence, we fitted an Ogden material model based on previously published experimental data and from the Mooney-Rivlin material relation and applied isogeometric Kirchoff-Love shells on this case.

The result of the wrinkling case, which was also modeled using commercial finite element codes, show that large deviations between commercial finite element codes are observed. The results of our model are in good agreement with the Hughes-Liu shells (reduced and full integration) in LS-DYNA. Furthermore, it was found that the Mooney-Rivlin model provides more accurate results to the experimental results than the Ogden material model, although their fits in the restrained tension test are similar. Based on the variation between the results from the Ogden and Mooney-Rivlin material models and the results obtained from LS-DYNA and ANSYS, we conclude that the results for this benchmark are sensitive to differences in element assumptions. This motivates the future use of this case as a challenging benchmark problem.

As a topic for future research, we suggest to develop analytical projection and direct decoupling [7] methods of the constitutive equations in order to prevent numerical through-thickness integration (i.e. eigenvalue computations for all through-thickness Gaussian points). These improvements could lead to a significant reduction of computational times.

References

[1] E. Cerda, K. Ravi-Chandar, L. Mahadevan, Wrinkling of an elastic sheet under tension, Nature (2002).
[2] E. Cerda, L. Mahadevan, Geometry and Physics of Wrinkling, Physical Review Letters (2003).
[3] A. Panaitescu, M. Xin, B. Davidovitch, et al., Birth and decay of tensional wrinkles in hyperelastic sheets, Physical Review E (2019).
[4] T. Wang, C. Fu, F. Xu, et al., On the wrinkling and restabilization of highly stretched sheets, International Journal of Engineering Science (2019).
[5] C. Fu, T. Wang, F. Xu, et al., A modeling and resolution framework for wrinkling in hyperelastic sheets at finite membrane strain, Journal of the Mechanics and Physics of Solids (2019).
[6] F. Xu, E. L. Johnson, C. Wang, et al., Computational investigation of left ventricular hemodynamics following bioprosthetic aortic and mitral valve replacement, Mechanics Research Communications (2020).
[7] F. Roohbakhshan, R. A. Sauer, Efficient isogeometric thin shell formulations for soft biological materials, Biomechanics and Modeling in Mechanobiology (2017).
[8] G. A. Holzapfel, R. Eberlein, P. Wriggers, H. W. Weizsäcker, Large strain analysis of soft biological membranes: Formulation and finite element analysis, Computer Methods in Applied Mechanics and Engineering (1996).
[9] R. W. Ogden, Non-linear elastic deformations, 1997.
[10] P. Steinmann, M. Hossain, G. Possart, Hyperelastic models for rubber-like materials: Consistent tangent operators and suitability for Treloar's data, Archive of Applied Mechanics (2012).
[11] C. O. Horgan, J. G. Murphy, Limiting chain extensibility constitutive models of Valanis-Landel type, Journal of Elasticity (2007).
[12] H. Darijani, R. Naghdabadi, Hyperelastic materials behavior modeling using consistent strain energy density functions, Acta Mechanica (2010).
[13] G. Chagnon, J. Ohayon, J. L. Martiel, D. Favier, Hyperelasticity Modeling for Incompressible Passive Biological Tissues, in: Biomechanics of Living Organs: Hyperelastic Constitutive Laws for Finite Element Modeling, 2017.
[14] G. Marckmann, E. Verron, Comparison of hyperelastic models for rubber-like materials, Rubber Chemistry and Technology (2006).
[15] M. H. Shariff, Strain energy function for filled and unfilled rubberlike material, Rubber Chemistry and Technology (2000).
[16] G. Duffett, B. D. Reddy, The analysis of incompressible hyperelastic bodies by the finite element method, Computer Methods in Applied Mechanics and Engineering (1983).
[17] J. C. Simo, R. L. Taylor, Quasi-incompressible finite elasticity in principal stretches. continuum basis and numerical algorithms, Computer Methods in Applied Mechanics and Engineering (1991).
[18] F. Gruttmann, R. L. Taylor, Theory and finite element formulation of rubberlike membrane shells using principal stretches, International Journal for Numerical Methods in Engineering (1992).
[19] Y. Başar, M. Itskov, Finite element formulation of the Ogden material model with application to ruber-like shells, International Journal for Numerical Methods in Engineering (1998).
[20] T. Sussman, K. J. Bathe, A finite element formulation for nonlinear incompressible elastic and inelastic analysis, Computers and Structures (1987).
[21] S. Reese, S. Govindjee, A theory of finite viscoelasticity and numerical aspects, International Journal of Solids and Structures (1998).
[22] Y. Başar, Y. Ding, Shear deformation models for large-strain shell analysis, International Journal of Solids and Structures (1997).
[23] N. Büchter, E. Ramm, D. Roehl, Three-dimensional extension of non-linear shell formulation based on the enhanced assumed strain concept, International Journal for Numerical Methods in Engineering (1994).
[24] T. J. Hughes, J. A. Cottrell, Y. Bazilevs, Isogeometric analysis: CAD, finite elements, NURBS, exact geometry and mesh refinement, Computer Methods in Applied Mechanics and Engineering (2005).
[25] J. Kiendl, K.-U. Bletzinger, J. Linhard, et al., Isogeometric shell analysis with Kirchhoff–Love elements, Computer Methods in Applied Mechanics and Engineering (2009).
[26] D. Benson, Y. Bazilevs, M. Hsu, et al., Isogeometric shell analysis: The Reissner–Mindlin shell, Computer Methods in Applied Mechanics and Engineering (2010).
[27] S. Hosseini, J. J. C. Remmers, C. V. Verhoosel, et al., An isogeometric solid-like shell element for nonlinear analysis, International Journal for Numerical Methods in Engineering (2013).
[28] J. Kiendl, Y. Bazilevs, M.-C. Hsu, R. Wüchner, K.-U. Bletzinger, The bending strip method for isogeometric analysis of Kirchhoff–Love shell structures comprised of multiple patches, Computer Methods in Applied Mechanics and Engineering (2010).
[29] H. Casquero, L. Liu, Y. Zhang, et al., Arbitrary-degree T-splines for isogeometric analysis of fully nonlinear Kirchhoff–Love shells, Computer Aided Design (2017).
[30] K. Bandara, F. Cirak, Isogeometric shape optimisation of shell structures using multiresolution subdivision surfaces, Computer Aided Design (2018).
[31] J. Kiendl, M.-C. Hsu, M. C. Wu, et al., Isogeometric Kirchhoff–Love shell formulations for general hyperelastic materials, Computer Methods in Applied Mechanics and Engineering (2015).
[32] A. B. Tepole, H. Kabaria, K.-U. Bletzinger, et al., Isogeometric Kirchhoff–Love shell formulations for biological membranes, Computer Methods in Applied Mechanics and Engineering (2015).
[33] S. Morganti, F. Auricchio, D. J. Benson, et al., Patient-specific isogeometric structural analysis of aortic valve closure, Computer Methods in Applied Mechanics and Engineering (2015).
[34] M. C. Wu, R. Zakerzadeh, D. Kamensky, et al., An anisotropic constitutive model for immersogeometric fluid–structure interaction analysis of bioprosthetic heart valves, Journal of Biomechanics (2018).
[35] M. C. Hsu, D. Kamensky, Y. Bazilevs, M. S. Sacks, T. J. Hughes, Fluid–structure interaction analysis of bioprosthetic heart valves: significance of arterial wall deformation, Computational Mechanics (2014).
[36] A. J. Herrema, E. L. Johnson, D. Proserpio, et al., Penalty coupling of non-matching isogeometric Kirchhoff–Love shell patches with application to composite wind turbine blades, Computer Methods in Applied Mechanics and Engineering (2019).
[37] Y. Bazilevs, M.-C. Hsu, J. Kiendl, R. Wüchner, K.-U. Bletzinger, 3D simulation of wind turbine rotors at full scale. Part II: Fluid-structure interaction modeling with composite blades, International Journal for Numerical Methods in Fluids (2011).
[38] M. A. Crisfield, An arc-length method including line searches and accelerations, International Journal for Numerical Methods in Engineering (1983).
[39] P. Wriggers, J. C. Simo, A general procedure for the direct computation of turning and bifurcation points, International Journal for Numerical Methods in Engineering (1990).
[40] H. Verhelst, M. Möller, J. den Besten, M. Kaminski, F. Vermolen, Equilibrium Path Analysis Including Bifurcations with a Fully-Integrated Arc-Length Method Avoiding A Priori Perturbations, in: Proceedings of ENUMATH2019 Conference, 2020.
[41] G. Holzapfel, Nonlinear solid mechanics: A continuum approach for engineering, 2000.
[42] P. Wriggers, Nonlinear finite element methods, 2008.
[43] Y. Başar, D. Weichert, Nonlinear Continuum Mechanics of Solids, 2013.
[44] R. A. Sauer, T. X. Duong, On the theoretical foundations of thin solid and liquid shells, Mathematics and Mechanics of Solids (2017).
[45] P. J. Flory, Thermodynamic relations for high elastic materials, Transactions of the Faraday Society (1961).
[46] S. Klinkel, S. Govindjee, Using finite strain 3D-material models in beam and shell elements, Engineering Computations (Swansea, Wales) (2002).
[47] B. Jüttler, U. Langer, A. Mantzaflaris, et al., Geometry + Simulation Modules: Implementing Isogeometric Analysis, PAMM (2014).
[48] A. Mantzaflaris, An overview of geometry plus simulation modules, in: Mathematical Aspects of Computer and Information Sciences, 2020.
[49] M. Mooney, A theory of large elastic deformation, Journal of Applied Physics (1940).
[50] R. S. Rivlin, Torsion of a rubber cylinder, Journal of Applied Physics (1947).
[51] L. R. G. Treloar, The Physics of Rubber Elasticity, 1 ed., 1975.
[52] W. F. Lam, C. T. Morley, Arc-Length Method for Passing Limit Points in Structural Calculation, Journal of Structural Engineering (1992).
[53] Z. Zhou, D. Murray, An incremental solution technique for unstable equilibrium paths of shell structures, Computers & Structures (1995).
[54] E. Puntel, L. Deseri, E. Fried, Wrinkling of a Stretched Thin Sheet, Journal of Elasticity (2011).
[55] L. Zheng, Wrinkling of Dielectric Elastomer Membranes, Technical Report, 2008.
[56] V. Nayyar, K. Ravi-Chandar, R. Huang, Stretch-induced stress patterns and wrinkles in hyperelastic thin sheets, International Journal of Solids and

Structures (2011).
[57] T. J. Healey, Q. Li, R.-B. Cheng, Wrinkling Behavior of Highly Stretched Rectangular Elastic Films via Parametric Global Bifurcation, Journal of Nonlinear Science (2013).
[58] Q. Li, T. J. Healey, Stability boundaries for wrinkling in highly stretched elastic sheets, Journal of the Mechanics and Physics of Solids (2016).
[59] M. Taylor, K. Bertoldi, D. J. Steigmann, Spatial resolution of wrinkle patterns in thin elastic sheets at finite strain, Journal of the Mechanics and Physics of Solids (2014).
[60] F. Fujii, E. Ramm, Computational bifurcation theory: path-tracing, pinpointing and path-switching, Engineering Structures (1997).
[61] LS-DYNA®Keyword User's Manual Volume 1, Technical Report R11.0, Livermore Software Technology Corporation, 2018.
[62] ANSYS®Academic Research Mechanical, Release 19.1, Help System, SHELL181, Technical Report R19.1, ANSYS, Inc., 2019.